# The Influence of Pine Island Ice Shelf Calving on Basal Melting

**A. T. Bradley[1], D. T. Bett[1], P. Dutrieux[1], J. De Rydt[2], P. R. Holland[1]**

[1]British Antarctic Survey, High Cross, Madingley Road, Cambridge CB3 0ET, UK
[2]Department of Geography and Environmental Sciences, Northumbria University, Newcastle upon Tyne, UK.

**Key Points:**

- Melting of Pine Island Ice Shelf is sensitive to calving because of a seabed ridge beneath it which restricts warm water access to the shelf.
- The melt response to calving has a strong sensitivity to the cavity geometry and results primarily from circulation changes.
- Calving may be an important contribution to the ice-ocean sensitivity of the Antarctic Ice Sheet.

Corresponding author: Alexander T. Bradley, aleey@bas.ac.uk

**Abstract**

The combination of the Pine Island Ice Shelf (PIIS) draft and a seabed ridge beneath it form a topographic barrier, restricting access of warm Circumpolar Deep Water to a cavity inshore of the ridge, thus exerting an important control on PIIS basal ablation. In addition, PIIS has recently experienced several large calving events and further calving could significantly alter the cavity geometry. Changes in the ice front location, together with changes in ice thickness, might relax the topographic barrier and thus significantly change basal melt rates. Here, we consider the impact of past, and possible future, calving events on PIIS melt rates. We use a high-resolution ocean model to simulate melt rates in both an idealized domain whose geometry captures the salient features of PIG, and a realistic geometry accurately resembling it, to explore how calving affects melt rates. The idealized simulations reveal that the melt response to calving has a sensitive dependence on the thickness of the gap between PIIS and the seabed ridge and inform our interpretation of the realistic simulations, which suggest that PIIS melt rates did not respond significantly to recent calving. However, the mean melt rate increases approximately linearly with further calving, and is amplified by approximately 10% relative to present day once the ice front reaches the ridge-crest, taking less than one decade if calving maintains its present rate. This provides strong evidence that calving may represent an important, but as yet unexplored, contribution to the ice-ocean sensitivity of the West Antarctic Ice Sheet.

## Plain Language Summary

The seabed beneath Pine Island Ice Shelf – the floating extension of Pine Island Glacier – features a large ridge. The combination of this seabed ridge and ice shelf above it reduce the amount of relatively warm water that is able to reach the ice shelf, therefore restricting the amount of ice shelf melting that can take place. However, the ice shelf has also lost large sections from its front in recent years, in a process referred to as calving. In this paper, we investigate the combined effect of these two processes: how does calving affect the melt rates on Pine Island Ice Shelf? Using numerical simulations of the ocean flow beneath the ice shelf, we identify a potentially high sensitivity of melt rates to calving, depending on the cavity geometry. This sensitivity is primarily related to changes in the flow strength in the cavity inshore of the ridge. In addition, our simulations suggest that the melt rate will have an approximately linear dependence on the distance that the ice front retreats in further calving events. These results provide strong evidence that changes in the melting of ice shelves in response to calving might represent an important contribution to the response of West Antarctica in a changing climate.

## 1 Introduction

Pine Island Glacier (PIG), located in the Amundsen Sea sector of Antarctica, is one of the fastest changing glaciers worldwide. A sustained increase in ice discharge and surface velocity, as well as significant grounding line retreat, have been documented since satellite measurements began in the 1990s (Rignot et al., 2002; Rignot, 2008; Rignot et al., 2011; Mouginot et al., 2014; Gardner et al., 2018). PIG has experienced a 70% increase in grounding line ice flux and a close to doubling of surface velocity between 1974 and 2013 (Mouginot et al., 2014), while its grounding line retreated some 31 km at its centre between 1992 and 2011 (Rignot et al., 2014). Increased basal melting of Pine Island Ice Shelf (PIIS) – the floating extension of the PIG's grounded ice – has been implicated as a key driver of these changes (Shepherd et al., 2004; Pritchard et al., 2012; Rignot et al., 2019): ice shelves offer a resistive stress (commonly referred to as 'buttressing') that restrains the flow of grounded ice; increased basal melting can reduce ice shelf volume and thus the buttressing they are able to provide (Gudmundsson, 2013; Reese,

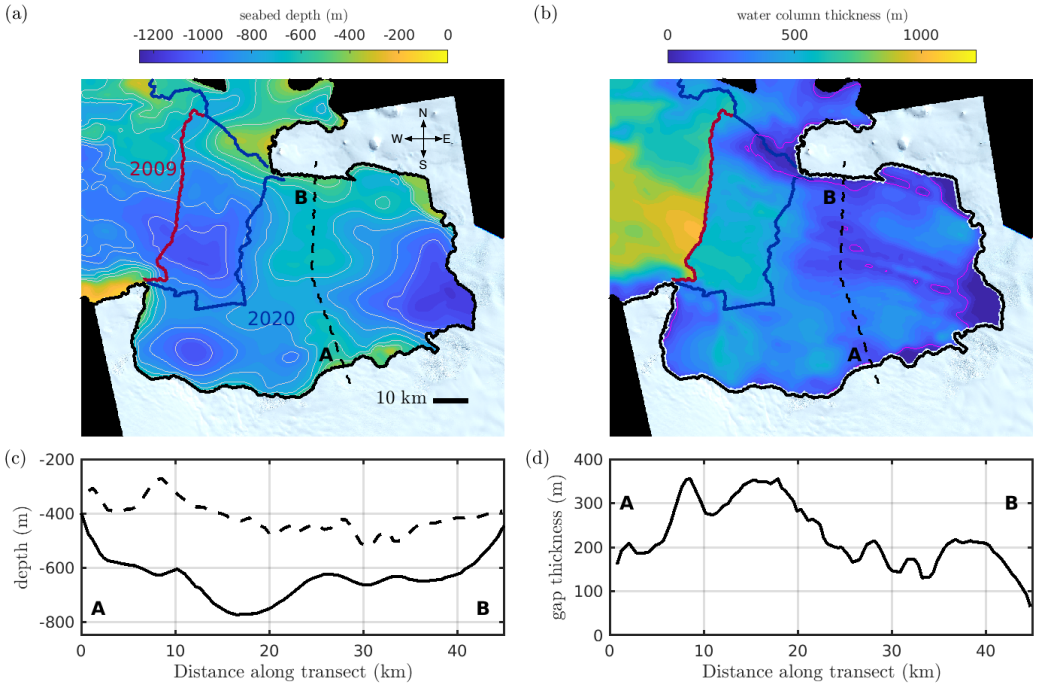


**Figure 1.** (a) Seabed depth and (b) water column thickness under Pine Island Ice Shelf and in Pine Island Bay (colors) from Dutrieux et al. (2014). Also shown are the locations of the ice front in 2009 (red line) and 2020 (blue line), as indicated in (a). The solid black line indicates the grounding line from Joughin et al. (2010), and the background image is a Sentinel 2 mosaic from November 2020 (ESA, 2020). The black dashed line indicates the approximate location of the crest of the seabed ridge. The magenta contour in (b) corresponds to 125 m water column thickness. (c) Seabed bathymetry (black solid) and ice draft (black dashed) taken along the black dashed line in (a)–(b). (d) Plot of the ridge-draft gap measured along the black dashed line in (a)–(b) [i.e. the difference between the solid and dashed lines in (c)].

Gudmundsson, et al., 2018; Gudmundsson et al., 2019; Gagliardini et al., 2010; Goldberg et al., 2019; De Rydt et al., 2021).

In the Amundsen Sea sector, Circumpolar Deep Water (CDW) provides the main source of heat that drives ice shelf melting. In this region, the pycnocline that separates CDW from Winter Water (which sits above the CDW) remains mostly above the level of the continental shelf break (Jacobs et al., 2015; Heywood et al., 2016). CDW is therefore able to spill onto the continental shelf and reach ice shelf cavities, providing significant heat to the adjacent ice shelves for melting. The flux of CDW that is able to spill over the continental shelf is a good proxy for the depth of this pycnocline; this flux (and thus the depth of the pycnocline) is not constant, but varies significantly on decadal timescales (Jenkins et al., 2018), as well as on seasonal and interannual timescales (St-Laurent et al., 2015; Webber et al., 2017, for example). Years with a deeper average pycnocline depth, and thus thinner average CDW layer thickness, tend to result in lower annual meltwater fluxes from ice shelves, and vice versa for years featuring a shallower pycnocline depth (Jacobs et al., 2011; Dutrieux et al., 2014).

However, for PIG specifically, this simple 'pycnocline depth' picture is complicated by the presence of a seabed ridge in the ice shelf cavity. This ridge is located several tens

of kilometers downstream of the grounding line, and protrudes up to three hundred meters above the neighboring seabed (figure 1a). In combination with the ice shelf directly above it, the ridge acts as a topographic barrier, restricting the access of CDW to an inner cavity which has formed between the ridge and the ice shelf since the grounding line retreated from this ridge in a process initiated in the late 1940s (Jenkins et al., 2010; De Rydt et al., 2014; De Rydt & Gudmundsson, 2016; Smith et al., 2017). This cavity geometry means that, at present, the strength of the topographic barrier, i.e. how much its presence affects ice shelf melting, is strongly dependent on the pycnocline depth: at its shallowest, the pycnocline sits above the depth of the ridge crest, and a large amount of modified CDW is able to spill into the inner cavity (Dutrieux et al., 2014); in contrast, at its lowest, the pycnocline sits some way below the ridge crest and CDW access is severely restricted. The presence of the seabed ridge thus contributes to the strong sensitivity of PIIS melting to hydrographic conditions in Pine Island Bay (PIB): Dutrieux et al. (2014) reported that the total freshwater flux from the fast flowing part of PIG in 2009 (80 $km^3$), when the pycnocline was at its shallowest depth on record (Webber et al., 2017), was more than double the total freshwater flux in 2012 (37 $km^3$), when the pycnocline was at the second-lowest recorded depth.

In addition to its topographic control on melt rates, the recent calving of PIIS also stands out amongst Amundsen Sea terminating ice shelves. The ice front of PIIS retreated approximately 26 km between 2009 and 2020 (figure 1a), with the majority of this retreat happening over the period 2015–2020 (Lhermitte et al., 2020; Joughin et al., 2021). This corresponds to a more-than-doubling of the calving rate, from approximately 4 km $year^{-1}$ prior to 2015, to approximately 9 km $year^{-1}$ in the period 2015–2020 [the flow speed at the ice front, for context, is approximately 5 km $year^{-1}$ (Joughin et al., 2021)]. Mass loss from the Antarctic ice sheet is dominated by calving and melting (Rignot et al., 2013), with equilibrium maintained when these losses balance the upstream accumulation of ice; the recent retreat of the ice front of PIIS, however, suggests that the calving rate is far higher than would be required to maintain an equilibrium.

As of 2020, the ice front is located approximately 20 km downstream of the ridge (figure 1a), meaning that the ice front is now closer to the ridge crest than it is to the location of the ice front in 2009. The immediate loss of buttressing associated with this ice front retreat can explain the acceleration of PIG since 2015 (Joughin et al., 2021). However, given that the topographic barrier to CDW relies on the combination of ice draft *and* seabed ridge, the recent calving events beg the following question: has recent calving of PIIS relaxed the topographic barrier, leading to significant changes in melting? Increased melting of its ice shelf might lead to further reductions in ice shelf volume and thus reduced buttressing on longer timescales, ultimately leading to ice shelf acceleration, thinning, and grounding line retreat.

In addition to considering the effect on melt rates of calving events that have already happened, one might also consider how melt rates might respond to possible future calving events. It has been suggested that further significant calving of PIIS is likely, since damage to the ice shelf that has already occurred is thought to have preconditioned PIIS to collapse (Lhermitte et al., 2020). In addition, there is evidence (Pettit et al., 2021) that the neighboring Thwaites ice shelf, which features similar damage and crevasse features to PIG, could collapse within as little as five years. Ice shelf thinning can enhance the calving rate of an ice shelf (Liu et al., 2015). Therefore, if calving does indeed affect melting, there is the potential for a 'calving-melting' positive-feedback loop in which ice shelf calving enhances melting and the resulting thinning promotes further calving. Here we test the first link in this chain: does calving enhance melting?

We also suggest for the first time the possibility of a a calving-melting feedback loop which occurs via damage: should calving enhance ice shelf melting, this may lead to reduced buttressing and the resulting ice acceleration (Gudmundsson et al., 2019, for example) might enhance ice shelf damage (Sun et al., 2017, for example) and thus precon-

dition the shelf for further calving (Lhermitte et al., 2020, for example). There is strong evidence for each step in this chain (indicated by the references) except for the first, whose possibility is assessed here.

In this study, we assess how, and why, melt rates on PIIS might respond to past, and possible future, calving events. To do so, we use the Massachusetts Institute of Technology general circulation model (MITgcm) (Marshall et al., 1997) to simulate the ocean circulation in, firstly, an idealized setup, the geometry of which captures the salient characteristic features of PIIS and its cavity (most notably, a seabed ridge whose crest is in proximity to the ice shelf base), and, secondly, a realistic setup, the geometry of which closely matches real world conditions for PIIS. We begin in §2 with a description of the idealized experiments, setting out details of the MITgcm and the experimental setup. We identify one such experiment as a baseline, and present the results of this experiment in §3. In §4, we describe how, and why, the melt rate varies as calving proceeds from this baseline, focusing in particular on the individual roles of changes in boundary layer speed and thermal driving in the changes to melt rates, following the approach of Millgate et al. (2013). In the following two sections, we discuss how the picture of melt response to calving presented in §4 changes when the cavity geometry (§5) and far field ocean conditions (§6) are altered. In §7 we describe and present the results of the realistic experiments. Guided by the results of the idealized experiments, we then assess the expected response of melt rates under PIIS to recent, and possible future, calving events. Finally, we discuss the implications of our results in §8, and summarize the key results in §9.

## 2 Idealized Experiment Details

In this section, we describe the experiments performed in an idealized setup, which we refer to as 'idealized experiments'. The idealized experiments have essentially the same setup as De Rydt et al. (2014), albeit it with an updated model configuration, and sections of the ice shelf removed to simulate calving. The domain features a seabed ridge and ice shelf (see figure 2a), which are both uniform in the zonal direction (and thus so too is the ridge-draft gap between them). In reality, however, the ridge-draft gap under PIIS is non-uniform (figure 1c–d); to capture the effect of this variation, we consider the melt response to calving for different thicknesses of the ridge-draft gap. We also consider several different far-field ocean conditions ('hydrographic forcings'): as discussed in §1, PIIS melt rates have a sensitive dependence on the hydrographic forcing, via the depth of the pycnocline; we therefore postulate that the melt response to calving might similarly have a sensitive dependence on the hydrographic forcing, and investigate this effect. The role of these idealized experiments, with a highly simplified geometry, is to allow us to isolate the important roles that the thickness of the ridge-draft gap and the hydrographic forcing play in the melt response to calving, as well as to elucidate the physical mechanisms responsible for these changes.

We perform a total of 90 idealized experiments, each corresponding to a unique triplet of parameters which respectively capture the thickness of the ridge-draft gap, the hydrographic forcing, and the position of the ice front. These parameters are described in the following two sections. By systematically shifting the ice front towards the (fixed) grounding line between experiments, we simulate calving, and we use that name to describe this procedure, but stress that our model includes neither calving dynamics, nor associated processes such as mélange formation. Within each experiment, we solve for the three-dimensional ocean circulation and associated melt rates simultaneously using the MITgcm. Other than removing sections of the ice shelf, the ice shelf geometry does not change between experiments. Ice shelves themselves enter the ocean model only via the exchange of heat and salt at the ice-ocean interface and a steady pressure loading on the ocean surface; in particular, ice dynamics are not taken into consideration when determining the cavity geometry. A steady description of ice shelves is sufficient to assess the response of melt rates to ice shelf calving, since the changes in melt rate follow-

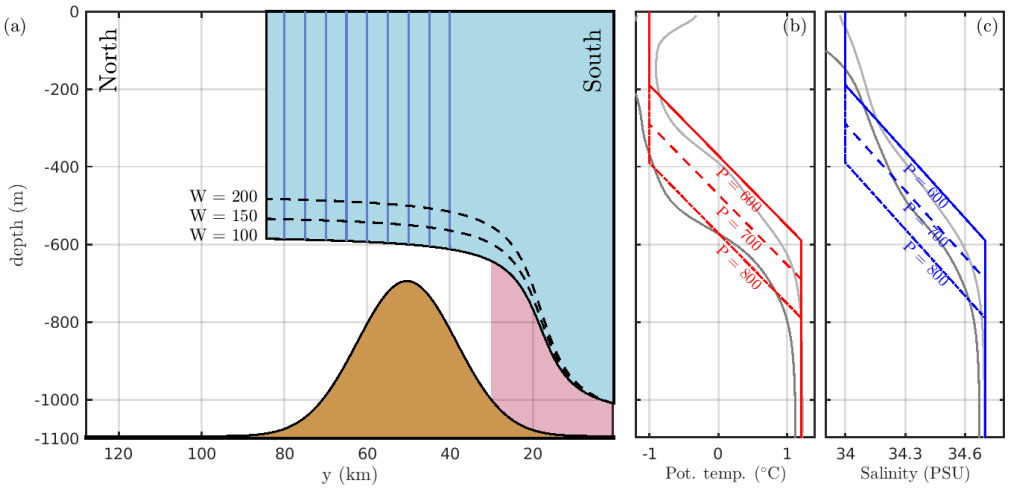


**Figure 2.** (a) Schematic diagram of the experimental setup. The domain is uniform in the zonal direction (into the page), with extent 48 km. The ocean domain consists of the gridded area, which is bordered by a static ice shelf in $y < 84$ km (shaded blue) and a seabed (shaded brown), which features a prominent ridge. Solid, dashed and dot-dashed black curves indicate the location of the ice shelf base for $W = 100$ m, $W = 150$ m, and $W = 200$ m, respectively, as labelled [the profile of the ice shelf base is defined in equation (4)]. Solid blue lines indicate the series of ice front positions considered, which are located at 84, 80, 75, 70, 65, 60, 55, 50, 45, and 40 km offshore of the southern end of the domain at $y = 0$ km (the $y$-axis is oriented in this way for consistency with the orientation of PIG in practice, see figure 1). The shaded red region indicates the inner cavity, defined as the area within 30 km of the southern end of the domain. (b) Temperature and (c) salinity profiles used in the experiments. Different line styles correspond to different values of the pycnocline depth parameter $P$ as follows: $P = 600$ m (solid), $P = 700$ m (dashed), $P = 800$ m (dot-dashed). Light and dark gray lines correspond to temperature and salinity profiles taken from conductivity, temperature, and depth measurements in Pine Island Bay during the austral summers of 2009 (Jacobs et al., 2011) and 2012 (Dutrieux et al., 2014), respectively.

ing calving occur on a timescale much shorter than that on which the ice geometry responds to perturbations in melting. In the following sections, we provide further details of the ocean model and experimental setup, including the motivation for our choices of parameters.

### 2.1 Details of Ocean Model

The MITgcm is a z-level general circulation model which includes a partial-cell treatment of topography, allowing an accurate description of the geometries of both the seabed and ice draft. Our model grid consists of 110 layers with a vertical spacing of $\mathrm{d}z = 10$ m, and a horizontal resolution of $\mathrm{d}x = 400$ m. We use the MITgcm in hydrostatic mode with an implicit nonlinear free surface scheme, a third-order direct space-time flux limited advection scheme, and a non-linear equation of state (McDougall et al., 2003). The Pacanowski-Philander (Pacanowski & Philander, 1981) scheme parametrizes vertical mixing. Constant values of 15 and 2.5 $\mathrm{m}^2\ \mathrm{s}^{-1}$ are used for the horizontal Laplacian viscosity and horizontal diffusivity, respectively. The equations are solved on an $f$-plane with $f = -1.4 \times 10^{-4}\ \mathrm{s}^{-1}$.

In each experiment, the MITgcm is run for twelve months, using a timestep of 30 seconds. After this spin-up time, the configuration is in quasi-steady state. For all experiments considered here, the melt rate is within 95% of its final value everywhere in the domain after at most three months. All results presented here are averaged over the final two months of the simulations.

As mentioned, ice shelves impact on the ocean state via the exchange of heat and salt at the ice-ocean interface. This exchange is described in the MITgcm using the so-called 'three-equation formulation' (Holland & Jenkins, 1999), which parameterizes heat and salt fluxes through the mixed turbulent boundary layer that forms adjacent to the ice-shelf base, but is not resolved in the MITgcm using the resolution considered here. The implementation of the three-equation formulation in MITgcm has been described thoroughly elsewhere (Losch, 2008; De Rydt et al., 2014; Dansereau et al., 2014, for example) and so we do not describe it in detail here. It is useful to note, however, that thermal exchange across the ice-ocean interface is typically dominated by latent heat [over heat conduction into the ice (Holland & Jenkins, 1999)]; in the case of negligible heat conduction, the three-equation formulation for melting reduces to

$$\dot{m} = \frac{c_p \gamma_T \Delta T}{L}. \tag{1}$$

In (1), $\dot{m}$ is the melt rate, $\Delta T = T - T_b$ is the thermal driving, with $T$ the temperature in the mixed layer adjacent to the ice base and $T_b$ the temperature at the ice shelf base, which must be at the local (depth and salinity dependent) freezing point. The quantity $\gamma_T$ is a heat exchange-coefficient, which parametrizes exchange between the mixed layer and the ice shelf base, and $c_p$ is specific heat capacity of the ocean water. In our version of the MITgcm, we assume that $\gamma_T$ has a linear dependence on $u^*$ (Holland & Jenkins, 1999), the ocean speed in the mixed layer. We can therefore write

$$\dot{m} \propto u^* \Delta T. \tag{2}$$

We shall return to equation (2) when diagnosing the mechanisms responsible for the melt rate response to ice shelf calving. In all results shown here, $u^*$ and $\Delta T$ are determined as the mean over a distance dz (the thickness of one grid cell) from the ice shelf base, as is standard in the MITgcm.

We use parameter values from Holland and Jenkins (1999) in (1)–(2), except for the drag coefficient in the three-equation formulation of melting, which is set to $4.5 \times 10^{-3}$. This value of the drag coefficient is tuned so that the simulated total meltwater flux in the realistic experiments using a geometry closely matching that of PIG in 2009

(described further in §7) is in line with the total meltwater flux for 2009 estimated by Dutrieux et al. (2014) based on observations (the simulated total meltwater flux is 86 $km^3$ $year^{-1}$ while the Dutrieux et al. (2014) estimate is 80 $km^3$ $year^{-1}$).

### 2.2 Ice Shelf Geometry and Seabed Bathymetry

The geometry of the idealized setup is shown schematically in figure 2a. It is uniform in the zonal direction, along which the $x$-axis is aligned, and the $y$-axis is aligned along the meridional direction. Note that although PIG is aligned approximately east-west (figure 1), we orient this idealized model north-south, as is standard (Grosfeld et al., 1997; De Rydt et al., 2014) and the results are independent of this choice of orientation.

The seabed has a shifted Gaussian profile,

$$b(x,y) = -1100 + 400 \exp\left[-\frac{\left(y - 50\times10^3\right)^2}{2\sigma^2}\right], \tag{3}$$

where $\sigma = 12$ km is the length scale over which this profile decays towards zero. The profile (3) corresponds to a ridge that peaks at a height of 400 m above the background bathymetry, which is at a depth of -1100 m. This peak occurs 50 km from the southern end of the domain at $y = 0$ km, which we consider to be the grounding line (figure 2a).

In reality, the variability in both PIIS draft and the height of the seabed ridge result in a ridge-draft gap that varies between approximately 100 m at its thinnest to more than 300 m at its thickest (figure 1c–d). Since we use the same, zonally uniform, seabed geometry (and, in particular, the same ridge height) in all of our idealized experiments, we aim to gain insight into the effect of variation in the ridge-draft gap by considering several different values of $W$ – the vertical distance between the crest of the seabed ridge and the ice shelf base (figure 2a). In our setup, $W$ enters the model only via the ice shelf draft profile; following De Rydt et al. (2014), we use an ice shelf draft given by

$$H(x,y) = \begin{cases} \left(\frac{310+W}{2.64}\right)\tan^{-1}\left(\frac{y}{5882} - 3\right) & \text{for } y < y_f, \\ 0 & \text{for } y \geq y_f. \end{cases} \tag{4}$$

Here $y_f$ is the variable location of the ice front (see below). In the following, we suppress the $x$ dependence of $b$ and $H$ to reflect their zonal uniformity.

We stress that the ice draft profile (4) is not obtained from ice dynamics considerations, but selected for its qualitative similarity to PIIS: it includes a flatter section offshore of the ridge and a steeper section inshore of the ridge, thus resembling variations in the basal slope that have been inferred from radar and satellite data (De Rydt et al., 2014). Note that the combination of the bathymetry (3) and ice shelf draft (4) means that the water column thickness is small, but nonzero at the grounding line (figure 2a); this is because the MITgcm requires at least two grid cells in the vertical direction to permit horizontal transfer.

We consider three different values of $W$ here: $W = 100$ m, $W = 150$ m, and $W = 200$ m. The smallest value, $W = 100$ m, corresponds to the minimum observed ridge-draft gap under PIIS (figure 1d), while the largest value, $W = 200$ m, corresponds to an upper bound above which there is little melt response to calving, as we shall see.

As mentioned, the front position $y_f$ is systematically reduced between experiments to simulate calving. We consider a total of ten different ice front positions, using $y_f =$ 84, 80, 75, 70, 65, 60, 55, 50, 45, and 40 km, which correspond to calved lengths of $l_c = 84 - y_f = 0$, 4, 9, 14, 19, 24, 29, 34, 39, and 44 km, respectively. Those experiments with $l_c = 0$ km are referred to as 'uncalved' experiments, serving as a benchmark against which results for $l_c > 0$ km are compared. There are both pragmatic and physical reasons for choosing this particular range of values for $l_c$: the setup with $\ell_c = 0$ km has

an ice shelf whose length is approximately equal to the observed distance of the ice front from the PIG grounding line in 2009, before significant calving took place in the late 2010s; the largest value, $l_c = 44$ km, is chosen as a compromise between allowing us to consider scenarios in which the ice front has been retreated significantly beyond the ridge, whilst retaining a large area that is shared by each experiment (as we discuss further in §3, the area over which melt rates are averaged must the same for each ice front position if we are to have a robust assessment of the melt response to calving).

### 2.3 Hydrographic Forcing

For each unique value of $W$ and $l_c$, we perform three experiments, each with a different hydrographic forcing. The range of these hydrographic forcings covers that which has been observed in practice (see below). Comparing the results of these experiments gives us an indication of the sensitivity of our results to hydrographic forcing.

The hydrographic forcing is imposed on the model by means of a restoring boundary condition at the northern end of the domain ($y = 128$ km in figure 2a): at this boundary, the temperature and salinity are restored to specified vertical profiles, shown in figures 2b and c, respectively, over a distance of five horizontal grid cells (total length 2 km) with a restoring timescale that varies from 12 hours at the boundary to 60 hours in the interior. The specified temperature and salinity profiles are piecewise linear functions of depth: they are constant in both an upper (temperature $-1°$C, salinity 34 PSU, corresponding to Winter Water) and lower layer (temperature 1.2°C, salinity 34.7 PSU, corresponding to CDW), which are separated by a pycnocline of 400 m thickness, across which the temperature and salinity vary linearly. The pycnocline begins at a variable depth $P$ (a higher $P$ corresponds to a deeper pycnocline), which parametrizes the entirety of the temperature and salinity profiles (figure 2b, c); the three hydrographic forcings we consider have $P = 600$ m, 700 m, and 800 m.

These piecewise linear profiles are approximations to typical conditions for PIB (Jacobs et al., 1996; Dutrieux et al., 2014; Jenkins et al., 2018) (figure 2b–c). As mentioned, the record of hydrographic conditions in PIB has revealed significant variability in the depth of the pycnocline on interannual timescales (Dutrieux et al., 2014); the profiles with $P =$ 600 m and $P = 800$ m are approximations to profiles observed in PIB in the the austral summers of 2009 and 2012, respectively (figure 2b, c). These two observations approximately span the range of observed conditions: in the 2009 observation, the average depth of the pycnocline was at its shallowest level on record, while in the 2012 observation the average depth of the pycnocline was at its second-deepest level on record (Webber et al., 2017). It should also be noted, however, that these observations have a significant seasonal bias, having been taken in austral summer. Since the pycnocline depth may vary significantly on interannual timescales, this range of observations represents a lower bound on possible observed conditions: in practice, there may have been hydrographic conditions occurring in PIB in the austral winter, or prior to the observational record, which are more extreme than these 2009 and 2012 austral summer observations. However, we restrict ourselves here to the range of $P$ values suggested by available observations.

In summary, we perform a total of 90 idealized experiments, with each uniquely identified by a ($W$, $P$, $l_c$) triplet, where $W \in \{100,\ 150,\ 200\}$ m, $P \in \{600, 700, 800\}$ m, and $l_c \in \{0,\ 4,\ 9,\ 14,\ 19,\ 24,\ 29,\ 34,\ 39,\ 44\}$ km. We consider the experiment with $W = 100$ m, $P = 600$ m, and $l_c = 0$ km to be the baseline; this corresponds to the extreme scenario with the narrowest ridge-draft gap (the strongest topographic barrier), the hydrographic forcing with the shallowest pycnocline (thickest CDW layer), and an uncalved ice shelf. In the following section, we describe the results of the baseline experiment. In §4, we describe the results of applying the calving perturbation to the baseline, presenting results of those experiments with $W = 100$ m, $P = 600$ m, $l_c > 0$ km; i.e. we describe the melt response to calving for $W = 100$ m, $P = 600$ m. In §5 and

§6, we respectively describe how the melt response to calving changes for the different values of $W$ and $P$ considered here.

## 3 Results for the Baseline Experiment ($W = 100$ m, $P = 600$ m, $\ell_c = 0$ km)

In this section, we describe the baseline experiment with $W = 100$ m, $P = 600$ m, which correspond to the solid lines in figure 2, and $l_c = 0$ km. Before we proceed, we introduce the 'inner cavity' – the area of the ocean domain that is located within 30 km of the grounding line (the southern boundary), which is indicated by the red-shaded region in figure 2a. We use the mean melt rate in the inner cavity, referred to henceforth as the 'inner cavity melt rate', as a single metric to quantify changes in melt rate with calving. Since the melt rate is highly spatially variable (see below) it is necessary to consider a fixed area that is common to each experiment when assessing changes in melt rate with calving. Indeed, averaging over the whole shelf, for example, would make smaller shelves appear to have anomalously large melt rates, since the region of high melt close to the grounding line would occupy a greater proportion of the entire shelf. Our choice of 30 km in this definition reflects a compromise between enabling simulations in which the ice front is retreated a significant distance beyond the ridge to be included (the smallest shelf we consider must be larger than the inner cavity, if the entirety of the inner cavity is to be included in each experiment), and considering a reasonably large section of the uncalved ice shelf over which the melt rate is averaged. Crucially, this choice includes the region adjacent to the grounding line, where changes in melt rate are particularly important for the dynamics of the grounded ice sheet (Seroussi et al., 2014; Arthern & Williams, 2017). Although the absolute values of the inner cavity melt rate *are* dependent on the length of region chosen in its definition, we verified that the trends and key results presented here are independent of this choice.

Ice-ocean properties that characterize the baseline simulation are shown in figure 3. Melt rates (figure 3a) are below 20 m year$^{-1}$ everywhere, except for within 20 km of the grounding line, where the melt rate reaches a maximum of 120 m year$^{-1}$. The average melt rate over the whole shelf is approximately 20 m year$^{-1}$; while this is lower than the value of 33$\pm$2 m year$^{-1}$ that was estimated by Jenkins et al. (2010) based on observations in PIB in 2009 (to which the $P = 600$ m case corresponds), this discrepancy is in the expected direction: the baseline simulation corresponds to the extreme scenario in which the ridge-draft gap is set everywhere to the minimum gap that is observed in practice, impeding the supply of warm water across the ridge. While the circulation is vigorous everywhere inshore of the ridge, high melt rates are restricted to the area south of $y = 20$ km because a cold and fresh meltwater plume sits adjacent to the ice-ocean interface north of $y = 20$ km(figure 3f), which results in a thermal driving that is much smaller to the north of $y = 20$ km than to the south it, where the ice is adjacent to warm water [the melt rate is approximately proportional to the product of the ice-ocean mixed layer circulation and thermal driving, see equation (2)].

When the ice shelf is calved in the subsequent simulations, the only a priori imposed change on the experiment is the water column thickness in those regions of the domain in which the ice shelf is removed (the resulting buoyancy forcing also changes but this emerges from the simulation a posteriori, rather than being imposed). It is therefore instructive to consider the effect of changes in water column thickness on the flow structure, which have influence only through the depth-averaged dynamics. We shall therefore study the changes in the depth-averaged flow structure as calving proceeds to elucidate the mechanisms responsible for the melt response to calving. We refer to this procedure as using a 'depth-averaged framework', but stress from the outset that we make no assumption that the flow structure itself is depth-independent (indeed, it can be seen in figure 3f that the water column is highly stratified). As we show below, the leading order change in the circulation in response to calving is that of the depth-averaged flow

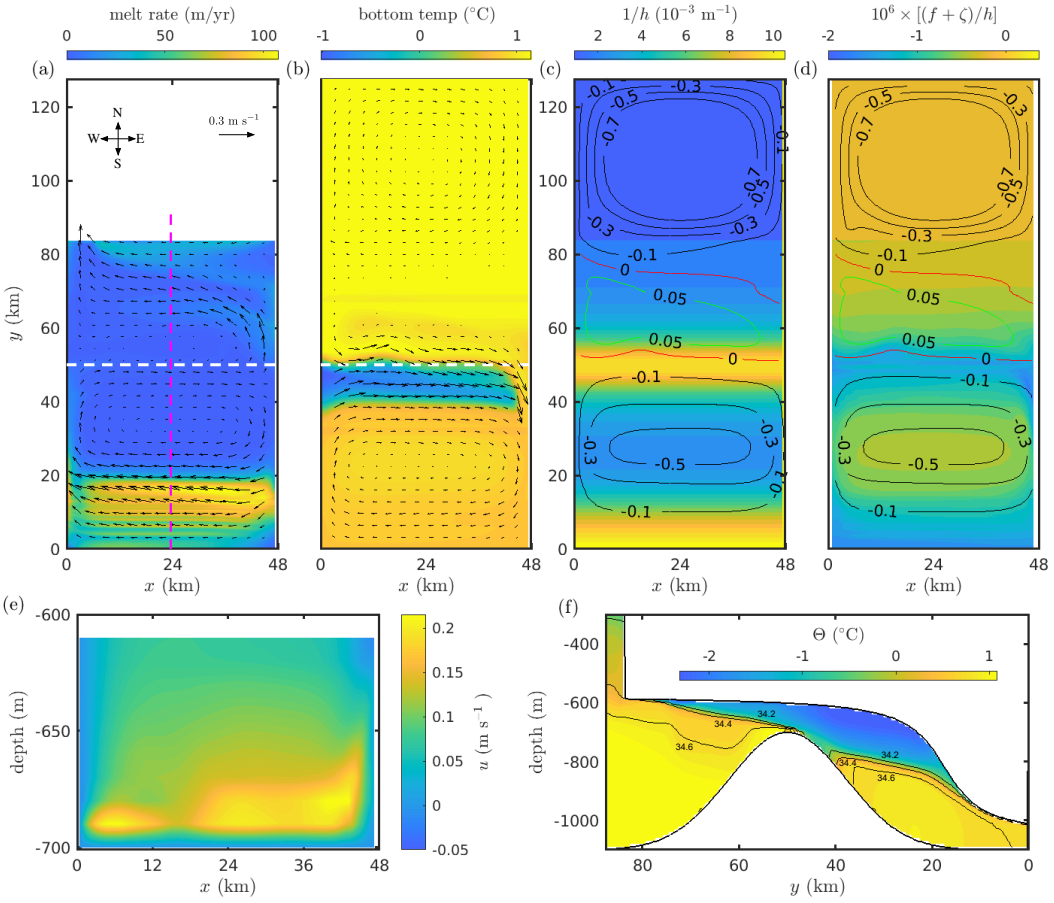


**Figure 3.** Ice-ocean properties in the baseline experiment ($W = 100$ m, $P = 600$ m, and $\ell_c = 0$ km). (a) Melt rate (colors) and ocean velocities (arrows, every fifth velocity vector is plotted), averaged over the three grid cells adjacent to the ice-ocean interface. Empty areas correspond to open ocean. The white dashed line indicates the location of the ridge crest, along which the section in (e) is taken, and the magenta dashed line indicates the center line $x = 24$ km, along which the section in (f) is taken. (b) Ocean temperature (colors) and velocity (arrows) averaged over the three grid cells closest to the seabed. The scale bar for velocity vectors in (a) is also appropriate for (b). (c) Inverse water column thickness $1/h$ and (d) barotropic potential vorticity (colors) alongside barotropic stream function (contours) at levels 0.05 (green) 0 (red), -0.1, -0.3, -0.5, and -0.7 Sv (all black). (e) Zonal cross-section taken at the ridge crest up to the ice shelf base, showing the signed meridional speed. (f) Meridional cross-section showing potential temperature (colors) and salinity contours at the 34.2, 34.4, and 34.6 PSU levels, as indicated, taken along the centerline $x = 24$ km.

and, additionally, changes, in the circulation strength are primarily responsible for the melt response, which justifies focusing on the depth-average flow structure.

When considering depth-averaged flow structure, it is common to appeal to either the barotropic potential vorticity (BPV) equation or the barotropic vorticity (BV) equation (Mertz & Wright, 1992; Jackson et al., 2006; Patmore et al., 2019). The BV equation is obtained by depth integrating the linearized momentum equations and then taking the curl, yielding an equation involving the relative vorticity of the depth averaged flow, $\hat{\zeta} = \partial\bar{v}/\partial x - \partial\bar{u}/\partial y$, where $u$ and $v$ are the components of the velocity in the $x$ and $y$ directions, respectively, and overbars denote depth-averages. The BV equation expresses depth-integrated northward mass flux as the sum of terms relating to nonlinear vorticity advection, surface and bottom stresses, viscous stresses, and the bottom pressure torque (Jackson et al., 2006).

In this paper, however, we focus on the BPV equation. This equation is obtained similarly, albeit with operations performed in a different order: the BPV equation is obtained by first taking the curl of the momentum equations and then depth averaging, which yields an equation including the depth average of the relative vorticity, $\zeta = \overline{\partial v/\partial x} - \overline{\partial u/\partial y}$. The BPV equation reads (Patmore et al., 2019)

$$\frac{\nu}{h}\nabla^2\zeta + \frac{1}{\rho_0 h}\mathbf{k}.\nabla\times\left(\frac{\tau_w-\tau_b}{h}\right) = \frac{\mathrm{D}}{\mathrm{D}t}\left(\frac{f+\zeta}{h}\right) \tag{5}$$

$$\approx \bar{v}f\frac{\mathrm{d}}{\mathrm{d}y}\left(\frac{1}{h}\right) + (\bar{u},\bar{v})\cdot\nabla\left(\frac{\zeta}{h}\right) \tag{6}$$

where $h$ is the water column thickness. As the sea surface height anomaly is generally small in comparison with the undisturbed water column thickness, we can assume that $h$ is the difference between ice shelf draft and the seabed, i.e. $h = H - b$. In (5)–(6), $\rho_0$ is a reference density, $\tau_w$ is the surface stress, $\tau_b$ is the bottom stress, and $\mathbf{k}$ is the unit vector pointing in the upwards vertical. In addition, $f = 2\Omega\sin\theta$ is the Coriolis frequency, where $\Omega = 7.2921\times10^{-5}$ rad s$^{-1}$ is the rotation rate of the Earth and $\theta$ is the longitude. In practice, the relatively small size of the idealized domain means that $\theta$, and thus $f$, can be assumed constant. The approximation (6) results from this assumption, alongside that of a zonally uniform water column thickness, and steady state conditions. It should be noted that baroclinicity does not enter into the BPV equation (5), which considers only depth-averaged quantities; the BPV equation would be identical for an homogeneous, unstratified fluid (Mertz & Wright, 1992), but we do not make that assumption here. Thus baroclinic flow plays no role in depth-averaged flow across $f/h$ contours, which is described by the BPV equation.

As is standard, we refer to the the quantity $(f+\zeta)/h$ as the BPV, the terms on the left-hand side of (5) as viscous sources of BPV, and the first and second terms on the right-hand side of (6) as planetary and relative contributions to BPV, respectively.

Mertz and Wright (1992) and Jackson et al. (2006) expound upon the relative merits of the BV and BPV equations in detail. As mentioned, we choose to focus here on the BPV equation (5), rather than the BV equation, when diagnozing the melt response to calving in our depth-averaged framework. There are two reasons for doing so: firstly, the BPV equation clearly exposes the relative and planetary contributions to BPV, allowing them to be directly compared, while the BV equation does not. Secondly, the BPV equation includes the water column thickness explicitly, allowing us to directly assess its influence of changes in the melt response to calving (recall that the water-column thickness is the quantity affected when we change the cavity geometry). Our intention here is not to present a detailed potential vorticity balance of flow in ice shelf cavities, for which additional insight could be gained from the BV equation. Rather we simply aim to use the BPV equation to shed light on the important processes and mechanisms responsible for the melt response to calving. We hope that the present work provides motiva-

tion for future studies considering the potential vorticity budgets of ice shelf cavities, which are currently lacking in the literature.

The barotropic potential vorticity equation (5) implies that in steady, inviscid flow with no bottom or surface stress, a water column advected by the flow will conserve its BPV. In our idealized domain, the water column thickness is approximately uniform in the zonal direction, i.e. $h$ varies only in the meridional direction (figure 3c). Therefore, whenever depth-averaged flow travels in the meridional direction, it crosses $1/h$ contours, and another contribution is required to balance the resulting BPV production. This can be achieved by adjusting relative vorticity, $\zeta$, but in places where that balance cannot hold, viscous stresses intervene to complete the BPV balance. Plots of $1/h$ (figure 3c), $(f+\zeta)/h$ (figure 3d), and the depth-averaged stream function (also referred to here as the barotropic stream function, as is common) (figure 3c, d) allow us to determine where in our domain each of the terms in equation (5) play an important role. In regions where streamlines of depth-averaged flow (contours of constant barotropic streamfunction) follow east-west aligned contours of constant water column thickness (lines of constant color in figure 3c), relative and viscous sources of vorticity are small; where contours of constant BPV (lines of constant color in figure 3d) deviate from these east-west aligned $f/h$ contours, relative vorticity plays an important role; finally, viscous stresses play an important role where streamlines of depth-averaged flow (lines in figure 3d) deviate from contours of constant BPV.

The ice front and the seabed ridge are the two predominant discontinuities in the water column thickness, and therefore act as BPV barriers: in order to cross these features in a meridional direction, depth-averaged flow must either change its relative vorticity or be subject to viscous stresses. These BPV barriers divide the domain up into three regions: inshore of the ridge, offshore of the ridge (but under the ice shelf, referred to as the 'outer cavity'), and the open ocean. (Note that the barriers also block baroclinic currents, but we do not consider this effect, in accordance with our use of a depth framework.)

In the open ocean, the combination of boundary restoring to salty water at the region's northern boundary and ice shelf freshwater influx at its southern boundary tilts the isopycnals, resulting in a cyclonic circulation. Note that, except for in the vicinity of the ice front, the gyre in the open ocean has uniformly spaced streamlines (figure 3c): the flow is not faster along the lateral boundaries than it is on the north and south boundaries. This corresponds to a uniform relative vorticity, which is consistent with the approximately constant water column thickness in the interior of this region. At the ice front, there is a vertical wall. In any flow crossing this wall, relative vorticity cannot balance the planetary BPV contribution (the flow cannot gain or lose vorticity over a zero length scale). Instead, the requirement for sudden shear causes viscous terms [left-hand side of (5)] to arise: the depth-averaged flow uses viscous contributions to balance the planetary vorticity contribution as it crosses the ice front (seen as deviations between colors and contours in figure 3d). During the spinup, the gyre in the open ocean increases in strength up until the shear at the ice front generates enough viscosity to permit depth-averaged flow to cross the ice front. This allows the heat flux, which causes melting thus tilting the isopycnals, to be maintained.

The same competition between boundary restoring and ice shelf freshwater flux, means that the depth-averaged dynamics inshore of the ridge are also dominated by a large cyclonic gyre. It is interesting to note the subtle differences between the circulation in this region and that in the open ocean; these differences ultimately arise because north-south depth-averaged flow in the inner cavity requires contours of constant water column thickness to be crossed: another contribution to BPV is required to balance the associated planetary vorticity contribution. To see this, consider the south-west quadrant of the inner cavity: when the depth-averaged flow in this region is northward, into a thicker water column, the planetary source term is positive ($f < 0$, $\bar{v} > 0$, $\mathrm{d}(1/h)/\mathrm{d}y <$

0); one way in which a relative vorticity source can balance this with a negative value is if the flow gains cyclonic (negative) vorticity ($\bar{v} > 0$, $\partial\zeta/\partial y < 0$). This can be extended to the other quadrants: if the depth-averaged flow is heading southwards, then the sign of these terms switches, and if the depth-averaged flow is heading into a thinner water column, they switch again. As a result, the relative vorticity becomes more negative in the south-west and north-east quadrants, and less negative in the north-west and south-east quadrants. These changes explain why the depth-averaged flow is intensified on the eastern and western boundaries: the depth-averaged flow must intensify (streamlines converge) to produce the required relative vorticity changes, i.e. the meridional topography variation is concomitant with zonal intensification of the meridional depth-averaged flow.

The outer cavity sits between the two regions hosting strongly topographically constrained circulations to its north and south. There is little flow in this region: the anticyclonic circulation that forms there (figure 3c) is much weaker than that in the open ocean or inshore of the ridge. This flow is not strong enough to generate the shear, and thus vorticity, that would be required at the ridge crest to balance planetary vorticity in southward flow across it (note the zero depth-averaged contour at the ridge crest, figure 3b). Just offshore of the ridge, flow is directed eastwards, parallel to the ridge crest. Where this jet meets the eastern domain boundary, flow is able to cross the ridge, providing the region inshore of the ridge with warm water from offshore of the ridge (figure 3b, e). This flow into the cavity is subject to high shear stresses, as inferred from the strong vertical velocity gradients on the eastern boundary of the ridge crest (figure 3e). The total flux into the cavity across the entire ridge (approximately 0.01 Sv) is small in comparison with the typical barotropic fluxes in the cavity, which are on the order of 0.3 Sv (inferred from the streamlines of the baroclinic streamfunction, figure 3c), i.e. the boundary current flushing of the inner cavity is relatively weak in comparison with the inner cavity circulation.

In the absence of significant flow across the ridge, the inshore side of the ridge hosts meltwater, which is recirculated rather than flushed out. Warm CDW entering the region inshore of the ridge at the eastern boundary mixes with this meltwater as it crosses the ridge, causing it to be lightly modified, becoming modified CDW. As a result, the bottom temperature is slightly cooler (approximately 0.8°C) inshore of the ridge than offshore (approximately 1.3°C, figure 3b).

In summary, the baseline simulation has a strong BPV barrier which restricts depth-averaged flow from crossing the ridge, and this blocked barotropic component in turn reduces the flow of CDW into the inner cavity. Strong cyclonic gyres are spun up in the open ocean and in the region inshore of the ridge, while in the outer cavity, the circulation is weak: the two cyclonic gyres are dynamically disconnected from one another. A boundary current at the eastern end of the ridge crest, which is subject to high shear, provides a modest source of lightly modified CDW, and thus heat for melting, to the region inshore of the ridge. The hosting of cold meltwater on the ice-ocean interface inshore of the ridge means that high melt rates are restricted to a region just downstream of the grounding line. The viscous contribution to vorticity is the important term in completing the BPV budget when the water column thickness changes at the ice front, while relative vorticity balances BPV production associated with water column stretching inshore of the ridge.

## 4 Melt Response to Calving

In this section, we describe how, and why, the inner cavity melt rate responds when sections of the ice shelf are sequentially removed from the ice shelf in the baseline configuration. The inner cavity melt rate as a function of the calved length $l_c$ is shown in figure 4a. We see that, while the ice shelf front is located far offshore of the ridge ($l_c <$

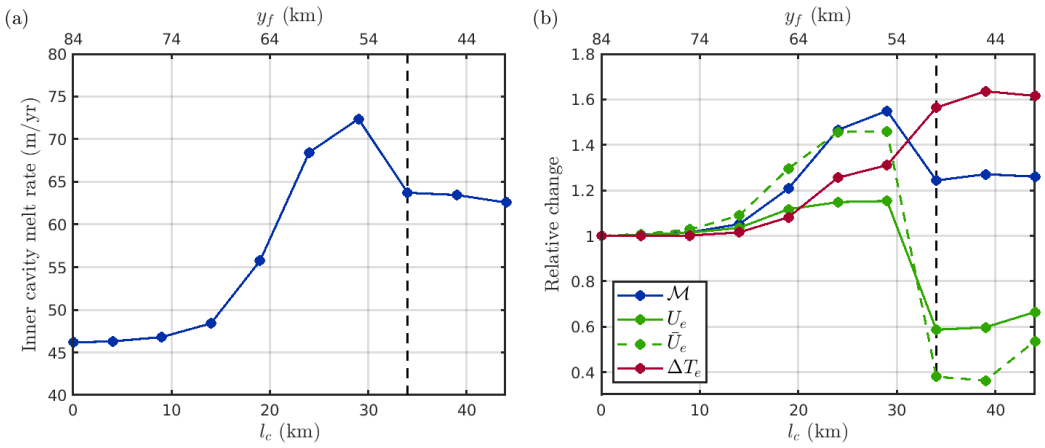


**Figure 4.** (a) Mean inner cavity melt rate as a function of the calved length $l_c$. The black dashed line indicates the position of the ice front when it is located directly above the seabed ridge. (b) Velocity-thermal driving decomposition: decomposition of changes in inner cavity melt rate relative to the baseline experiment into changes associated with boundary layer speed $U_e$ [green curve, equation (7)] and thermal driving $\Delta T_e$ [red curve, equation (8)]. The blue curve indicates the change in melting relative to the baseline (uncalved) experiment [equation (9)]. The green dashed line indicates the depth-averaged velocity effect $\bar{U}_e$ [equation (10)].

14 km), removing sections of ice results in a weak increase in the inner cavity melt rate. However, as the ice shelf front is retreated further towards the ridge, the melt rate increases more strongly with calving, reaching a maximum of 73 m year$^{-1}$ (70% larger than in the baseline simulation) when the ice shelf is located approximately 5 km north of the ridge crest. Perhaps surprisingly, retreating the ice front slightly further to sit directly above the ridge crest results in a significant decrease in the inner cavity melt rate of approximately 15% (from 73 m year$^{-1}$ to 64 m year$^{-1}$). Finally, the inner cavity melt rate is approximately independent of ice front position when the ice front is located inshore of the ridge ($l_c > 34$ km).

To understand the reasons for this melt response to calving, it is instructive to return to equation (2), which indicates that the melt rate is proportional to the product of the boundary layer speed and thermal driving. Guided by this equation, we can decompose changes in the inner cavity melt rate relative to the baseline simulation into changes in boundary layer speed and thermal driving by first computing (Millgate et al., 2013)

$$U_e(l_c) = \frac{\int_{\mathrm{IC}} u^*(x,y;l_c)\ \Delta T(x,y;l_c=0)\ \mathrm{d}x\mathrm{d}y}{\int_{\mathrm{IC}} u^*(x,y;l_c=0)\ \Delta T(x,y;l_c=0)\ \mathrm{d}x\mathrm{d}y}, \tag{7}$$

$$\Delta T_e(l_c) = \frac{\int_{\mathrm{IC}} u^*(x,y;l_c=0)\ \Delta T(x,y;l_c)\ \mathrm{d}x\mathrm{d}y}{\int_{\mathrm{IC}} u^*(x,y;l_c=0)\ \Delta T(x,y;l_c=0)\ \mathrm{d}x\mathrm{d}y}, \tag{8}$$

where 'IC' refers to the inner cavity. Recall that $u^*(x,y;l_c)$ and $\Delta T(x,y;\ell_c)$ are the boundary layer velocity and thermal driving, respectively, that emerge from the experiment in which the ice front is located at $y = l_c$, and are computed as the mean over a distance equal to the grid resolution $\mathrm{d}z$ from the ice shelf base. The quantities (7)–(8) are referred to as the 'boundary layer speed effect' and 'thermal driving effect', respectively. They are compared, for a given calved length $l_c$, to the quantity

$$\mathcal{M}(l_c) = \frac{\int_{\mathrm{IC}} u^*(x,y;l_c)\ \Delta T(x,y;l_c)\ \mathrm{d}x\mathrm{d}y}{\int_{\mathrm{IC}} u^*(x,y;l_c=0)\ \Delta T(x,y;l_c=0)\ \mathrm{d}x\mathrm{d}y}, \tag{9}$$

which is the relative change in melting over the baseline simulation.

Figure 4b shows the quantities (7)–(9) as a function of $l_c$. Here, a melt response to calving that results exclusively from changes in thermal driving would be indicated by indistinguishable blue and red curves, and a green curve that takes the value unity for all $\ell_c$; a melt response that results exclusively from changes in boundary layer velocity would be indicated by indistinguishable blue and green curves, and a red curve that takes the value unity for all $\ell_c$. Henceforth, we refer to this comparison as a 'velocity-thermal driving decomposition'.

The velocity-thermal driving decomposition (figure 4b) indicates that both changes in the boundary layer velocity and thermal driving play an important role in the melt response to calving, i.e. neither plays a dominant role. When the ice front is located offshore of the ridge ($l_c < 30$ km), ice front retreat results in increases in both the boundary layer velocity and thermal driving: these increases are complementary, acting in unison to increase the inner cavity melt rate as calving proceeds. When the calving front is retreated to sit above the ridge, the thermal driving effect increases further, while the velocity effect decreases sharply, corresponding to a significant reduction in the boundary layer velocity at this point. This reduction in cavity circulation outweighs the increase in thermal driving, leading to an overall reduction in the inner cavity melt rate. When the ice shelf is calved further beyond the ridge, both the thermal driving and boundary layer velocity effects are approximately constant.

As mentioned, we shall assess the impact of calving on the behaviour primarily by considering its effect on the depth-averaged flow structure. To that end, we consider also the 'depth-averaged velocity effect', $\bar{U}_e(\ell_c)$, which is computed as in (7) albeit with depth-averaged, rather than boundary layer, speeds:

$$\bar{U}_e(\ell_c) = \frac{\int_{\mathrm{IC}} |\bar{\mathbf{u}}(x,y;l_c)|\ \Delta T(x,y;l_c=0)\ \mathrm{d}x\mathrm{d}y}{\int_{\mathrm{IC}} |\bar{\mathbf{u}}(x,y;l_c=0)|\ \Delta T(x,y;l_c=0)\ \mathrm{d}x\mathrm{d}y}, \tag{10}$$

where $\bar{\mathbf{u}} = (\bar{u}, \bar{v})$ is the depth-averaged velocity.

The agreement between the trends of the $U_e$ and $\bar{U}_e$ curves (figure 4b) suggests that changes in boundary layer velocity are closely related to changes in depth-averaged speed, and provides support for our use of depth-averaged framework when diagnosing the melt response to calving.

We identify two regimes in the melt response to calving. In the first regime, the ice front is located offshore of the ridge, $\ell_c < 30$ km and the behavior is qualitatively similar to the uncalved case. In particualar, the strong BPV barrier provided by the ridge and ice draft remains in place, and depth-averaged flow is unable to cross the ridge. The modest transport of warm water across the ridge, towards the inner cavity, occurs primarily via an eastern boundary jet, and the cavity circulation is vigorous. A topographically constrained cyclonic circulation is spun up inshore of the ridge, and this remains disconnected from the cyclonic circulation that is spun up in the open ocean (figure 5a) because of the presence of a relatively stagnant outer cavity region.

As ice front retreat proceeds within this regime, the total meltwater flux from the shelf (the area integrated melt rate) reduces ($\ell_c = 0$–$29$ km in figure 5b). This reduction is the non-trivial outcome of a competition between a reduction in melting area and an increase in ocean temperature inshore of the ridge as the ice shelf front is retreated. On the one hand, a smaller ice shelf means a reduction in the area over which melting is applied, promoting a reduced meltwater volume. On the other hand, a reduction in meltwater leads to reduced mixing between the cold outflow and the warm inflow across the ridge, so the temperature of the warm water that enters the cavity increases, promoting an increased melt rate. In this case, the effect of reductions in shelf area slightly outweighs the associated increase in melt rate when determining the overall meltwater

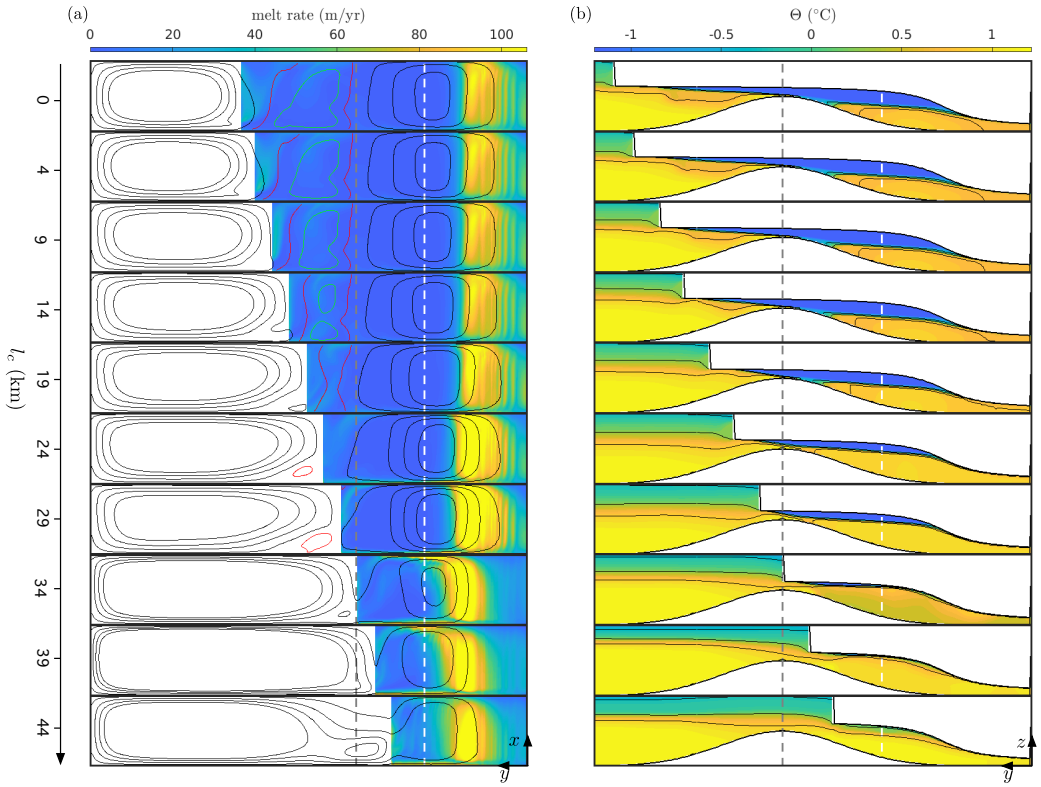


**Figure 5.** (a) Contour plots of melt rate (colors) and barotropic stream function (contours, black at -0.1, -0.3, -0.5, and -0.7 Sv levels, magenta at the 0 Sv level, and green at the 0.05 Sv level) in the idealized simulations with $P = 600$ m and $W = 100$ m. The calved length $l_c$ increases from 0 km in the first row to 44 km in the final row. The white sections indicate open ocean. The gray dashed line indicates the location of the ridge crest and the white dashed line indicates the extent of the inner cavity region [also in (b)]. (b) Contour plots of potential temperature $\Theta$ (colors) and salinity (contours, at levels 34.2, 34.4, and 34.6 PSU, i.e. as in figure 3) taken along the centreline of the domain. The white sections at the top and bottom of each subplot indicate the ice shelf and seabed ridge, respectively. In both cases, the color bar at the top of the column is appropriate for each row in the column.

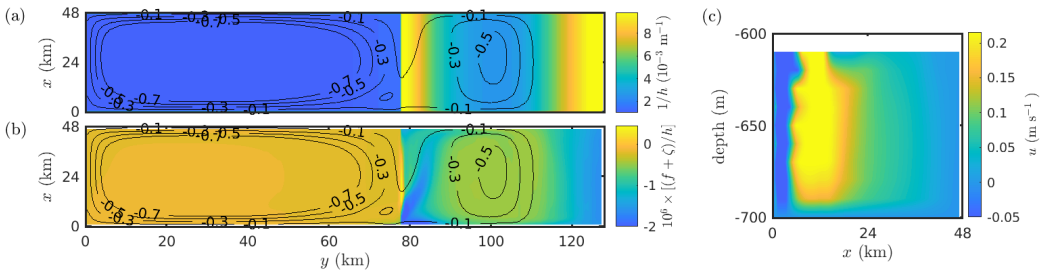


**Figure 6.** Contour plots of (a) inverse water column thickness $1/h$ and (b) barotropic potential vorticity $(f + \zeta)/h$ (colors) alongside barotropic stream function (black contours) at levels -0.1, -0.3, -0.5, and -0.7 Sv, as indicated, for the simulation in which the ice front is located directly above the ridge ($\ell_c = 34$ km). (c) Zonal cross-section of the meridional velocity taken at the ridge crest, up to the ice shelf base.

flux, and is consistent with an increase in the thermal driving for $\ell_c < 30$ km (figure 4b). The associated increase in melt rate in the inner cavity leads to a stronger buoyancy flux, driving a slightly stronger circulation (increase in $\bar{U}_e$ in figure 4b), which itself enhances melting locally.

The second regime takes effect when the ice front is located above the seabed ridge crest. In this case, only a single PV barrier – the ice front, which now sits at the ridge crest – remains. The region offshore of the ridge, which previously hosted a weak circulation that separated the strong cyclonic gyres in the open ocean and in the region inshore of the ridge, no longer exists, permitting these two gyres to connect dynamically (figure 6a–b). The flow at the ridge crest now has a vigorous barotropic component (figure 6c); north-south barotropic flow across the ridge is permitted because the planetary vorticity requirement associated with such flow can be satisfied by viscous sources associated with the ice front. It can be seen (figure 6a–b) that relative vorticity and viscous sources of BPV are small (contours of the depth-averaged streamfunction aligned with contours of constant water column thickness) everywhere except for at the ice front and at the domain boundaries. Furthermore, viscous stresses only play an important role in completing the BPV budget at the ice front (indicated by deviating BPV colours and depth-averaged streamfunction contours in figure 6b): the viscous contribution to vorticity is important at the ice front, while relative vorticity balances BPV production associated with water column stretching inshore of the ridge.

The satisfaction of the planetary vorticity requirement by viscous sources permits a depth-averaged flow of approximately 0.1 Sv to cross the ridge at its western side (figure 6), providing a large amount of heat to the inner cavity, while meltwater is efficiently flushed out of the cavity on the eastern side of the ridge (figure 6c). The region inshore of the ridge is almost entirely flooded with warm water (figure 5b); although this means that there is much more heat available for melting (thermal driving effect increases when the ice front coincides with the ridge crest, figure 4b), the more efficient cavity flushing leads to a concomitant reduction in circulation strength (figure 4b). The reduction in circulation strength outweighs the increase in thermal driving, ultimately leading to a reduction in the melt rate (figure 4a).

We can shed light on this reduction in circulation that occurs when depth-averaged flow is able to cross the ridge by considering the balance that must be struck between the heat source from the northern restoring boundary and the heat sink that results from melting. The melt rate (and its heat sink) is set by the local ocean temperatures and flow speeds, which in turn control the amount of heat that the wider circulation must supply from the northern boundary in order to be maintained. We can consider the system as two processes: in one process the heat is transferred from the inner-cavity to the ice to set the melt rate, and in the second, heat is transferred from the northern restoring boundary into the inner cavity, to supply the first process. The latter may be achieved by either vertical overturning or horizontal circulation. However, the horizontal circulation mode is the more efficient mode for transferring heat since it can accommodate shear over long (order 10 km) lengthscales, rather than the small (order 10 m) vertical scales on which shearing must occur in an overturning circulation. Additionally, horizontal transfer does not require density gradients or viscous processes (such as Ekman transport) or lateral boundary layers to facilitate it. When the ice front is located offshore of the ridge, heat is supplied to the inner cavity via a high-shear overturning circulation in a boundary layer, which might require a strong barotropic circulation inshore of the ridge to generate the steep density gradients and shear required to support it (figure 3e). However, once depth-averaged flow can cross the ridge, this heat is much more efficiently supplied to the inner cavity (figure 6c) by horizontal transfer, and a strong barotropic circulation is not required to facilitate heat provision.

This 'highly calved' picture remains when the ice front is retreated beyond the ridge. The gyres in the open ocean and in the region inshore of the ridge are connected, per-

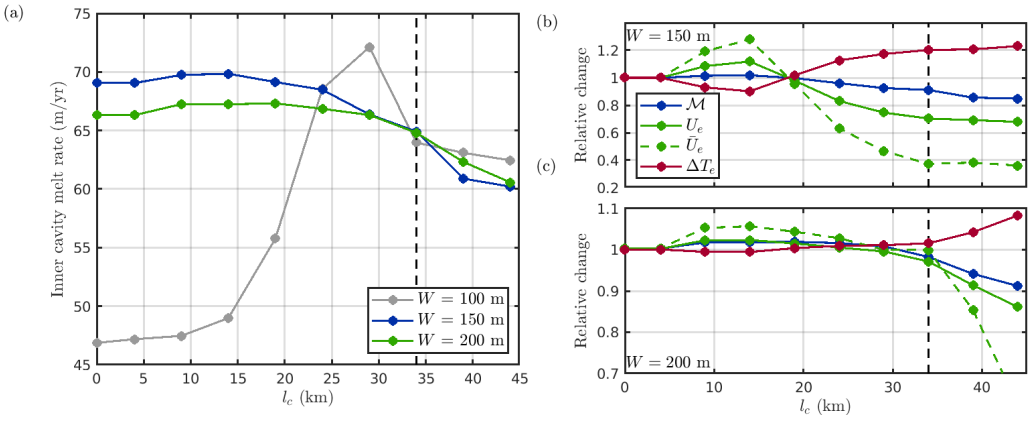


**Figure 7.** (a) Inner cavity melt rate as a function of the calved length $l_c$ for $W = 100$ m (grey, as in figure 4a), $W = 150$ m (blue), and $W = 200$ m (green), each with $P = 600$ m. (b)–(c) Velocity-thermal driving decomposition for (b) $W = 150$ m and (c) $W = 200$ m. In each plot, the black dashed line indicates the position of the ice front when it is located directly above the seabed ridge. The legend in (b) is also appropriate for (c).

mitting a significant depth-averaged flow to cross the ridge, which efficiently flushes the inner cavity with warm water. Thermal driving is enhanced, but cavity circulation is reduced, when compared to the situation in which the ice front is located offshore of the ridge. Melt rates become independent of ice front position once the ice front has retreated beyond the ridge, which indicates that the ridge only plays a role in the melt response to calving when it has an ice shelf overlying it (and the ridge-draft gap is small enough, as will be shown).

In summary, when the ice front is located offshore of the ridge, the ridge-draft BPV barrier prevents depth-averaged flow from crossing ridge and the inner cavity is weakly flushed with warm water via a high-shear boundary flow at the eastern wall. As the ice front retreats, mixing with meltwater at this boundary is reduced; the heat content, and thus melt rate, in the inner cavity increases, leading to enhanced circulation and further increasing melt. As the ice front is retreated to the ridge crest, viscous vorticity exchanges at the ice front permit depth-averaged flow to cross the ridge. This flow efficiently flushes the inner cavity with warm water, providing a large amount of heat for melting, but is accompanied by a reduction in cavity circulation. The reduction in circulation outweighs the increase in heat to ultimately reduce the inner cavity melt rate, compared to when the ice front is located offshore.

## 5 Effect of Cavity Geometry on Melt Response to Calving

In the previous section, we analyzed how the inner cavity melt rate responds to ice front retreat, and discussed the mechanisms responsible, in the case that the gap between the ice draft and ridge-crest is narrow. The strength of the topographic barrier that restricts warm water access to the inner cavity was identified as an important control on this response. In this section, we describe how this picture changes for larger values of $W$ (in particular, for $W = 150$ m and $W = 200$ m), which lead to a weaker topographic barrier at the ridge crest.

Figure 7a shows the inner cavity melt rate as a function of calved length $l_c$ for $W = 150$ m and $W = 200$ m in the $P = 600$ m case. We focus first on the $W = 200$ m case, which is characterized by inner cavity melt rates that are largely independent of

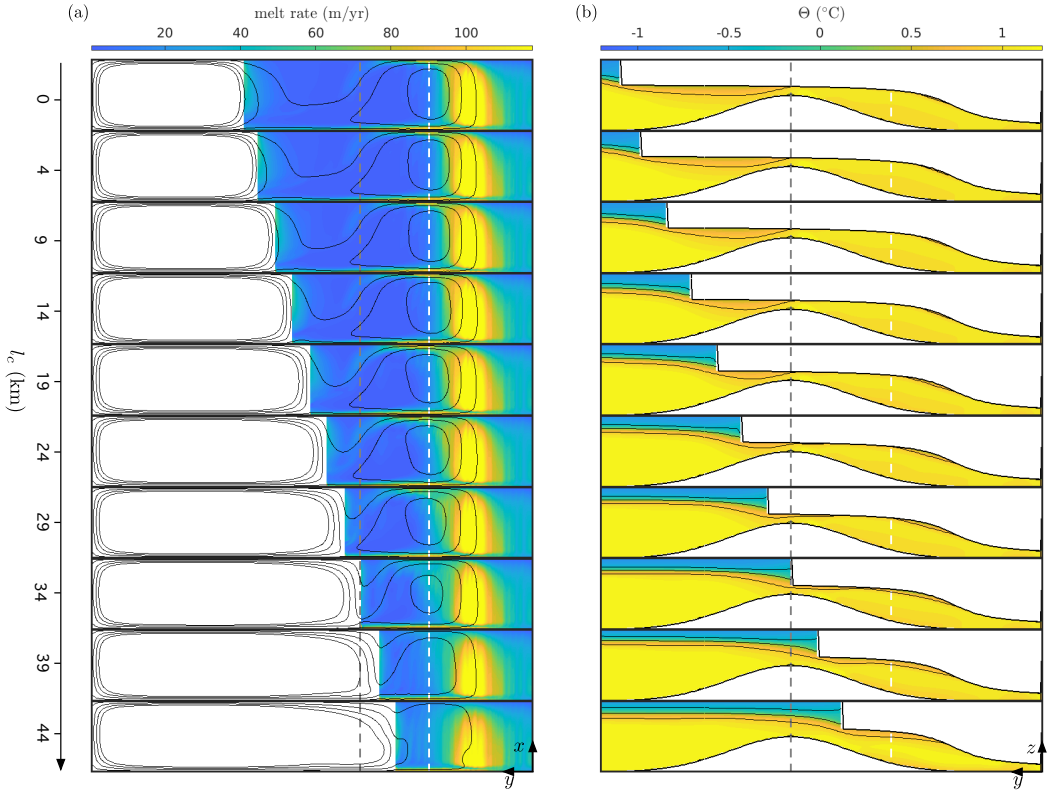


**Figure 8.** Response of ocean characteristics to calving in the idealized experiments with $P = 600$ m and $W = 200$ m. This plot is as in figure 5, albeit for the experiment with $P = 600$ m and $W = 200$ m. Note that in (a), the -0.7 Sv contour does not appear in the region inshore of the ridge for any value of $\ell_c$.

the ice front position. As before, we use a depth-averaged framework to diagnose the behavior, noting that in both the $W = 150$ m and $W = 200$ m cases, there is also strong correlation between boundary layer and depth average velocity effects (figure 7b–c), as in the $W = 100$ m case. Barotropic stream function contours are shown alongside meridional cross-sections for the $W = 200$ m case in figure 8 (the corresponding figure for $W = 100$ m is figure 5). Recall that in the $W = 100$ m case two regimes are observed, which are delineated by whether depth-averaged flow is able to cross the ridge or not: firstly, when the ice front is located offshore of the ridge, there is a 'blocked' regime in which the strong BPV barrier that the ridge-crest and ice draft presents means that depth-averaged flow is prevented from crossing the ridge and, secondly, when the ice front is located above, or inshore, of the ridge, there is a 'connected' regime in which the gyres in the open ocean and inshore of the ridge become dynamically connected and depth-averaged flow is able to cross the ridge. In the $W = 200$ m case, however, the BPV barrier at the ridge crest is much weaker than in the $W = 100$ m case, and depth-averaged flow is able to cross the ridge, even when the ice front is located offshore of the ridge (figure 8a). The blocked regime is never realized with $W = 200$ m: for all values of $\ell_c$, the regions inshore and offshore of the ridge are dynamically connected. The system behaves in a qualitatively similar way to the $W = 100$ m connected regime, with the inner cavity efficiently flushed with modified CDW (figure 8b), and experiencing weak circulation (figure 8a), regardless of the ice front position, and ice front retreat has little effect. In particular, this removes the tendency for both increasing temperature and circulation that we see in the $W = 100$ m case as the ice front is retreated towards the ridge. This invariance to ice front position also holds for larger ridge-draft gaps ($W > 200$ m), a finding that is consistent with the results of De Rydt et al. (2014).

The $W = 150$ m case has features in common with both the strong response end member case ($W = 100$ m) and the weak response end member case ($W = 200$ m). This case shares the following features with the $W = 100$ m case: there is a reasonable sensitivity to ice front position (although it is somewhat smaller than in the $W = 100$ m case), the inner cavity melt rate reaches a maximum when the ice front is located offshore of the ridge crest (figure 7a), and the reduction in inner cavity melt rate for values of $\ell_c$ above that at which the maximum melt rate is attained results from a reduction in the inner cavity circulation which outweighs an increase in thermal driving (figure 7b). In contrast to the $W = 100$ m case, however, this scenario does not display a threshold-like behavior in which the inner cavity melt rate drops suddenly as the calving front reaches the top of the ridge. The weaker BPV barrier in the $W = 150$ m case means that, as in the $W = 200$ m case, the blocked regime is never realized; the threshold behavior, which occurs at the transition between the two regimes, is therefore suppressed.

## 6 Effect of Hydrographic Conditions on Melt Response to Calving

Before moving on to assess how the inner cavity melt rate responds to calving in the realistic simulations, we briefly consider how the picture presented in the previous two sections changes depending on the choice of hydrographic forcing. Since we consider a constant ridge height, variations in the difference between the pycnocline depth and the height of the ridge crest, which we expect to be a key driver of the quantity of warm water that is able to spill over the ridge and into the inner cavity, is captured here by variability in the value of $P$ (figure 2).

The inner cavity melt rate and velocity-thermal driving decomposition for the experiments with $P = 700$ m (hydrographic forcing as in the dashed profiles in figures 2b and c) and with $P = 800$ m (dot-dashed profiles) are shown in figures 9a and b, respectively. The results for $P = 700$ m are similar to those for $P = 600$ m: for the narrowest gap ($W = 100$ m), the inner cavity melt rate is sensitive to the ice front position, increasing rapidly as the ice front is retreated towards the ridge crest, before dropping

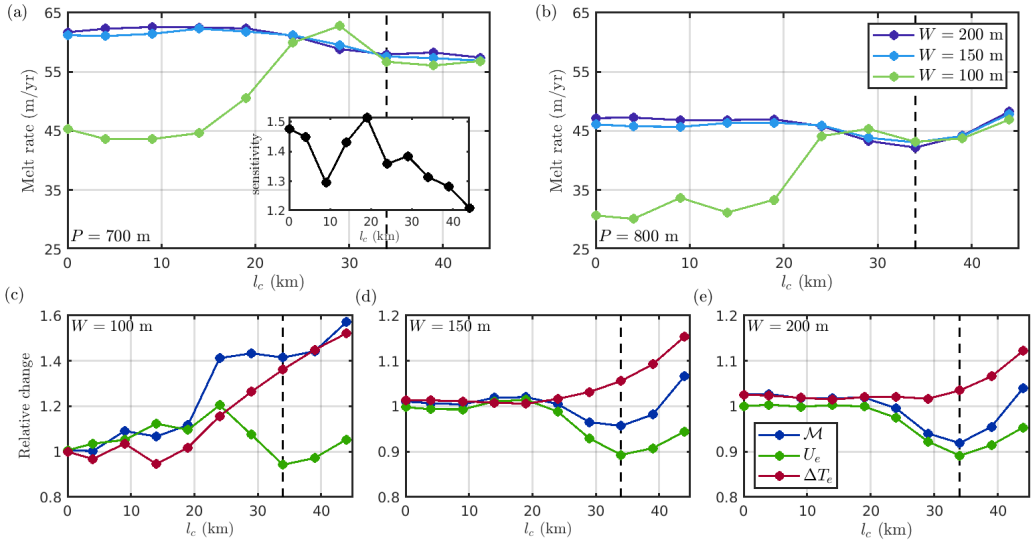


**Figure 9.** (a)–(b) Inner cavity melt rate as a function of calved length $l_c$ in idealized simulations with (a) $P$=700 m and (b) $P$=800 m. Colors correspond to different values of $W$, as indicated by the legend in (b). The black dashed line indicates the location of the crest of the seabed ridge. The inset in (a) shows the sensitivity to the pycnocline position – the ratio of the inner cavity melt rate for $P = 700$ m and $P = 800$ m [i.e. the ratio of the data represented by the green lines in (a) and (b))] – as a function of the calved length $l_c$. (c)–(e) Velocity–thermal driving decompositions for the $P = 800$ m data shown in (b): (c), (d), and (e) correspond to the results for $W = 100$ m, $W = 150$ m, and $W = 200$ m, respectively, as indicated.

off sharply when the ice front reaches it, and does not change under further ice front retreat beyond the ridge. In addition, the sensitivity of melt rate response to calving reduces as the gap widens. A velocity-thermal driving decomposition for the experiments with $P = 700$ m (not shown) is qualitatively similar to the $P = 600$ m case discussed above, suggesting that the mechanisms for the response are as discussed in §4. The similarity between the $P = 600$ m and $P = 700$ m cases is perhaps unsurprising when framed in terms of the relationship between the depth of the pycnocline and the height of the ridge crest: in both cases, the CDW layer extends all the way to the top of the ridge (see figure 2) and thus the seabed ridge alone does not provide a significant barrier to CDW access to the inner cavity.

In the $P = 800$ m case, while the ice front is located offshore of the ridge, the melt rate is either constant, or increases, as the ice front is retreated, depending on the value of $W$ (figure 9b). A reduction in the ice-ocean boundary layer velocity is responsible for a slight drop in inner cavity melt rates as the ice front is retreated towards the ridge crest (figure 9c–e), as in the $P = 600$ m and $P = 700$ m cases. Beyond this point, however, the $P = 800$ m case differs from the $P = 600$ m and $P = 700$ m cases: retreating the ice front beyond the ridge results in an increase in the inner cavity melt rate (figure 9b), which is associated with a reversal of the reduction in boundary layer velocity (figure 9c–e), i.e. the boundary layer velocity increases on average when the ice front is retreated beyond the ridge (however, it should be noted that despite this increase, the inner cavity melt rate in situations where the ice front has retreated beyond the ridge is still lower in the $P = 800$ m case than in the $P = 700$ m and $P = 800$ m cases, see figure 9a–b). The important difference in this case is that the seabed ridge alone is able to provide a significant barrier that prevents warm water from reaching the inner cavity; the

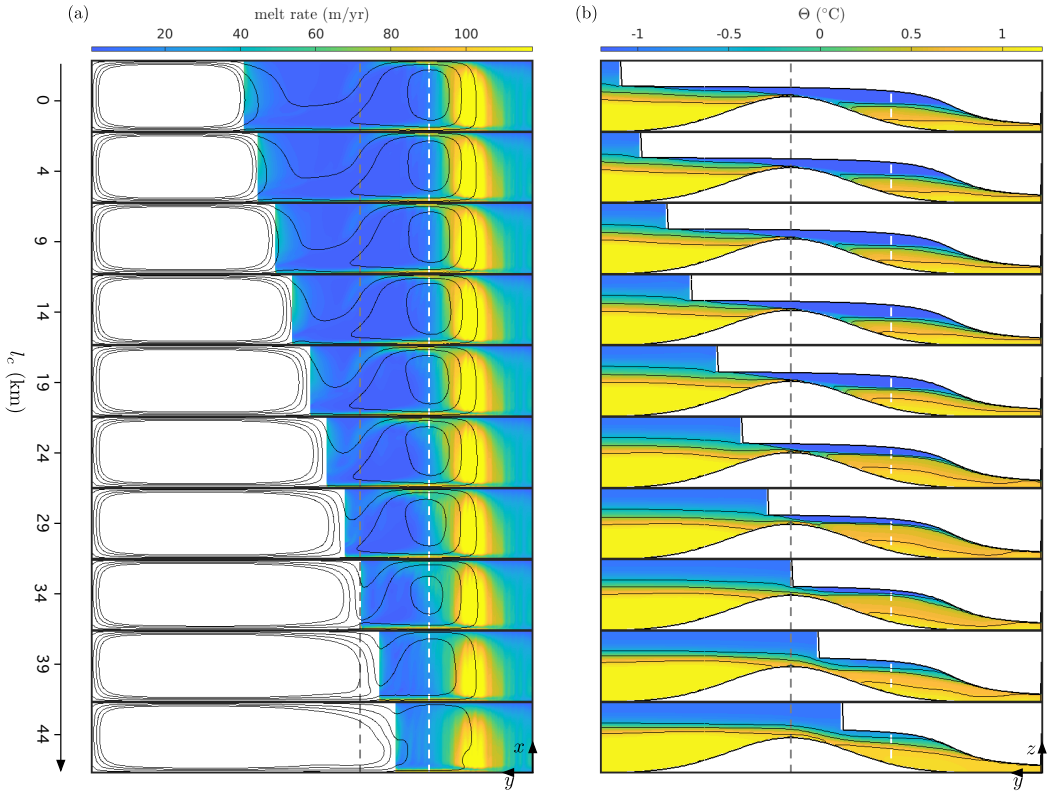


**Figure 10.** Response of ocean characteristics to calving in the idealized experiments with $P = 800$ m and $W = 200$ m. This plot is as in figure 5 for the experiment with $P = 800$ m, $W = 100$ m.

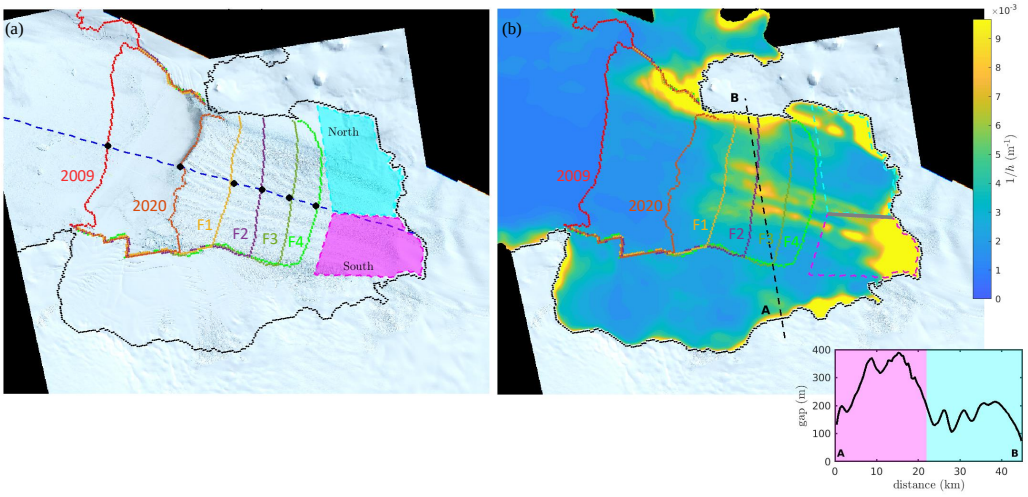


**Figure 11.** (a) Ice front positions used in experiments designed to assess the response of the PIIS melt rate to calving. Each experiment corresponds to a different ice front position: labelled red and orange ice fronts correspond to the 2009 and 2020 front positions, respectively, while the yellow, purple, dark green, and light green ice fronts labelled F1–F4 correspond to possible future ice front positions. The solid black line indicates the location of the 2009 grounding line from Joughin et al. (2010). The blue dashed line roughly indicates the centreline of the cavity, along which the calved length – the difference between the ice front in the respective experiments and the 2009 ice front – is measured. The cyan (north) and magenta (south) boxes indicate the inner cavity regions considered in the experiments (see main text). The background image is a Sentinel 2 mosaic from November 2020 (ESA, 2020). (b) Inverse water column thicknesses $1/h$ used in the experiment with the 2009 ice front. Ice front positions and inner cavity regions are as in (a). Note that the boundary between the inner cavity regions (indicated by a solid gray line) is approximately aligned with a region of locally enhanced $1/h$, indicating the presence of a topographic barrier between the northern and southern inner cavity regions. Inset: plot of the (vertical) gap between the ridge crest and the ice draft, measured along the black dashed line in the main figure. Cyan and magenta shaded sections correspond to locations north and south of the blue dashed centreline in (a), respectively.

CDW layer in the outer cavity does not extend over the top of the ridge (figure 10). As calving proceeds beyond the ridge, the thermal driving does not saturate (as in all the cases discussed above), but continues to increase, and the concomitant increase in glacial melt results in a stronger circulation (figure 9c).

## 7 Assessing the Melting Response of PIIS to Calving

The experiments described in §2–6 reveal how melt rates near the grounding line in idealized geometries with a uniform ridge-draft gap may respond sensitively to calving, with the sensitivity of response depending heavily on the thickness of the ridge-draft gap. These idealized experiments inform our understanding of similar experiments in a realistic domain, which are designed to assess the response of melt rates to PIIS calving. In this section, we describe these experiments, and present and analyze the results.

### 7.1 Experiment Details

Our experiments with a realistic setup are designed to assess the possible response of PIIS melt rates to calving in practice. To do so, we solve for the three-dimensional, quasi-steady ocean circulation and associated melt rates simultaneously in a PIG cavity geometry [from Dutrieux et al. (2014), and described briefly below], using the ocean model described in §2.1. In particular, we use the same grid resolution (400 m in the horizontal and 10 m in the vertical), timestep (30 seconds) and spin-up time (12 months) as in the idealized simulations. We consider six different ice shelf topographies, each of which has a unique ice front position. The locations of these ice fronts are shown in figure 11: the first experiment ('2009' labelled curve in figure 11a) uses an ice shelf geometry that corresponds to PIIS in 2009 (Dutrieux et al., 2014). The second experiment ('2020' labelled curve in figure 11a) uses the 2009 ice shelf draft, but with a section of ice removed so that the ice front matches that obtained in 2020, whose position was determined from a Sentinel 2 mosaic of PIG (ESA, 2020). The four further experiments (labelled F1–F4 in figure 11) similarly use the 2009 ice shelf draft but with sections of fast flowing ice (i.e. within the shear margins) removed (figure 11). We stress that, as in the idealized experiments, the ice thickness, and thus grounding line position and ice shelf draft, at existing shelf locations remains the same in each experiment, and only the ice front position varies.

The sub-ice shelf cavity geometry is computed from the ice and seabed geometry, as described by Dutrieux et al. (2014). Briefly, Dutrieux et al. (2014) calculated the ice shelf geometry from a 40 m-resolution digital elevation model (DEM) of the ice freeboard from 2008 (Korona et al., 2009), which was adjusted with a constant median bias from observations obtained from the Autosub underwater autonomous vehicle (Jenkins et al., 2010). This DEM assumes freely floating ice throughout the shelf, which may reduce its accuracy close to the grounding line. Over the continental shelf, the seabed geometry is well known from ship echo-sounding (Dutrieux et al., 2014), while in the cavity it was calculated from an inversion of gravimetry data and corrected point-wise using the median difference between the depth from the gravimetry inversion and the Autosub observations. We consider a single hydrographic forcing, corresponding to observed 2009 conditions in Pine Island Bay (dark grey lines in figure 2b–c), to which the ocean is restored far from the ice shelf.

The ridge-draft gap under PIIS is not uniform but varies from approximately 100 m at its narrowest to more than 400 m at its widest (inset in figure 11b). The ridge-draft gap can be approximately partitioned into a northern section, where the gap is relatively narrow, and a southern section, where the gap is relatively wide. A region of locally elevated $f/h$ running east-west (solid gray line in figure 11b) meets the approximately north-south aligned seabed ridge at the junction between these wide and narrow sections (see figure 11); this east-west aligned section is created by a thick ice keel in the center of the ice stream and extends all the way to the grounding line, partitioning the region inshore of the north-south aligned ridge into a northern inner cavity (cyan box in figure 11a) and a southern inner cavity (magenta box). The east-west aligned section of locally elevated $f/h$ provides a BPV barrier between the two inner cavity regions, which are therefore approximately dynamically disconnected (figure 12a). In the following, we therefore evaluate the melt response to calving in the two inner cavity regions separately.

### 7.2 Results

Cavity circulation (figure 12a) and melt rates (figure 13a) in the uncalved (2009) experiment are qualitatively similar to the corresponding baseline idealized experiment: melt rates are concentrated near to the grounding line, reaching a peak of approximately 120 m year$^{-1}$ several kilometers downstream of the grounding line, while remaining below 20 m year$^{-1}$ over the majority of the shelf. This pattern of simulated melt rates un-

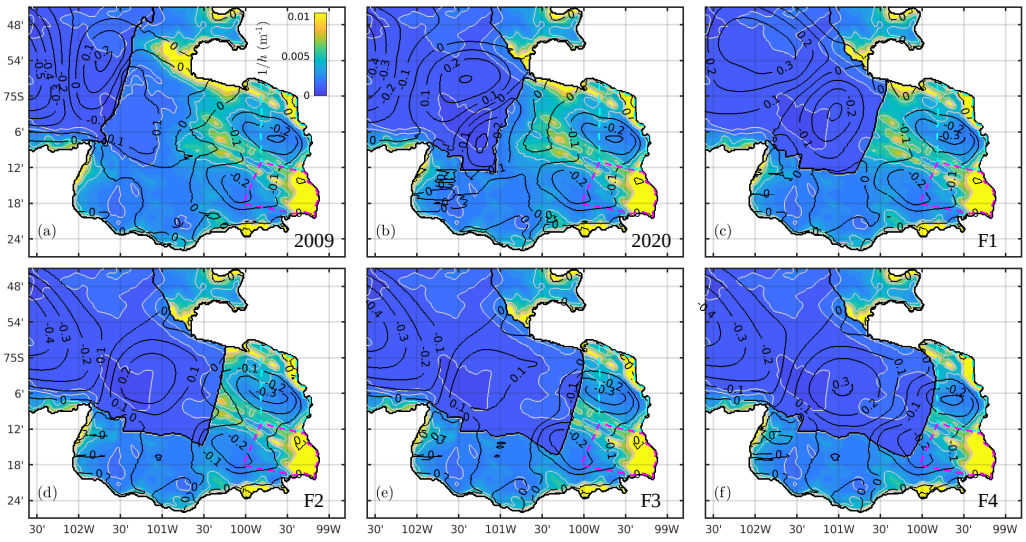


**Figure 12.** Simulated barotropic stream function (labelled black contours) and inverse water column thickness $1/h$ (colors and gray contours) in (a) the 2009 ice front scenario, (b) the 2020 ice front scenario and (c)–(f) the future ice front scenarios F1–F4. The gray contours correspond to water column thicknesses of 200, 400, 600, 800, and 1000 m and are simply intended to guide the eye around the background colormap. Magenta and cyan dashed boxes indicate the extent of the northern and southern inner cavity regions, respectively.

der PIIS is consistent with observations (Dutrieux et al., 2013) and other numerical simulations of cavity circulation under PIIS (Heimbach & Losch, 2012, for example). A cyclonic circulation spins up within both inner cavity regions, and in the open ocean offshore of the ice front, while a weak anti-cyclonic circulation spins up in the outer cavity between the seabed ridge and the ice front. Barotropic stream function contours largely follow the contours of constant water column thickness (figure 12a).

Figures 13b–f show the melt rate anomalies relative to the previous front position: red (blue, respectively) locations on these maps indicate areas in which the melt rate increases (decreases) when the ice front is retreated from its position in the next largest ice shelf. When the ice front is retreated from its 2009 position to its 2020 position, melt rates within 10 km of the ice front increase significantly (figure 13b). This is attributed to high velocities associated with overcoming the topographic barrier at the new ice shelf front, as well as the formation of a reasonably strong gyre in the newly exposed open ocean, which is covered by the ice shelf in the 2009 configuration (figure 12b). This double gyre pattern is qualitatively similar to observations taken in PIB in 2020 (Yoon et al., 2022). The gyre adjacent to the ice shelf results in a strong circulation along the ice front and this stronger circulation promotes a higher melt rate which in turn provides a freshwater source to further enhance the local buoyancy forcing and thus flow speed. Melt rates in both inner cavity regions do not change significantly when the ice front is retreated from its 2009 position to its 2020 position: the average melt rate in the northern and southern regions increases by approximately 0.2 m year$^{-1}$ and 1.2 m year$^{-1}$ respectively (figure 14a, c).

Melt rates in the simulations with ice fronts retreated beyond the 2020 position display complex patterns of change, which include large regions of both positive and neg-

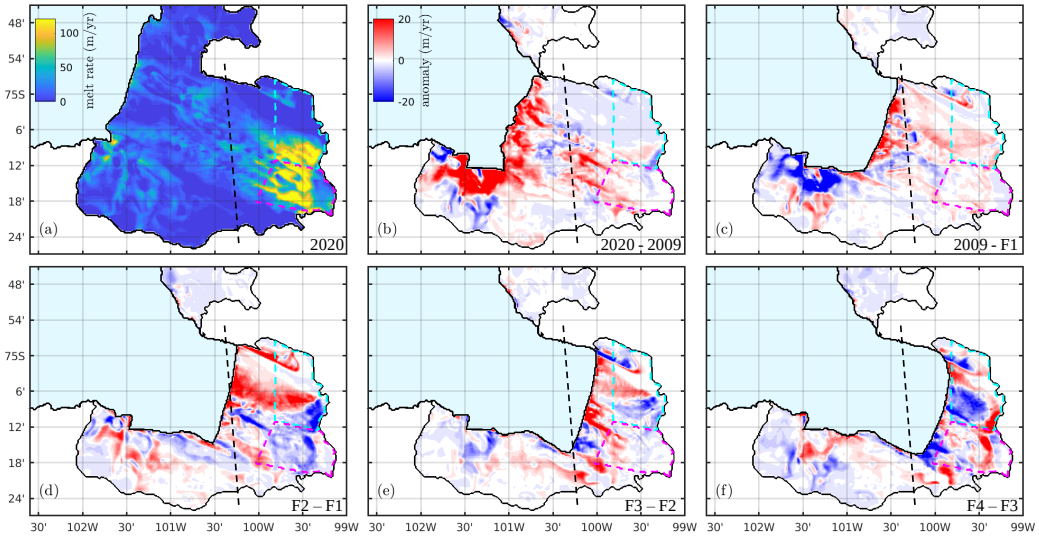


**Figure 13.** (a) Simulated melt rate in the 2009 Pine Island geometry. Cyan and magenta dashed boxes [also in (b)–(f)] indicate the northern and southern inner cavity regions (see figure 11), where the highest melt rates are concentrated. (b)–(f) Non-cumulative melt rate anomaly in the simulations (i.e. measured relative to the previous panel). The colorbar in (b) is appropriate for each of (b)–(f). Note that melt rate anomalies in (b) are saturated to a maximum of 20 m year$^{-1}$ in the vicinity of the ice front (the maximum anomaly is approximately 30 m year$^{-1}$). In each case, the ice shelf front and 2009 grounding line from Joughin et al. (2010) are shown as a solid black line, and an estimate of the location of the ridge crest is shown as a black dashed line.

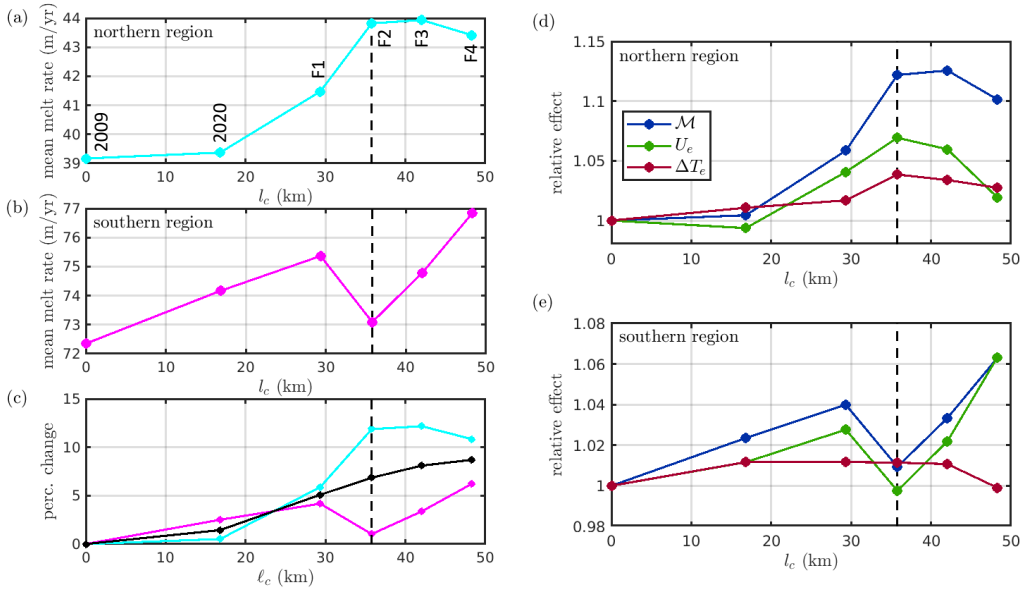


**Figure 14.** (a), (b) Average melt rate in (a) the northern inner cavity region (cyan box in figure 11) and (b) the southern inner cavity region (magenta box) of the PIG geometry as a function of calved length $l_c$. The distance $l_c$ is measured along the blue dashed line in figure 11a, taken relative to the 2009 ice front position (red front in figure 11a). (c) Percentage change in melt rate compared to the 2009 ice front experiment ($\ell_c = 0$ km) as a function of calved length $\ell_c$ for the northern inner cavity region (cyan curve), southern inner cavity region (magenta curve) and the entire inner cavity region (black curve). (d), (e) Velocity-thermal driving decomposition for the changes in melt rate shown in (a) and (b), respectively. As indicated by the legend in (d), blue, red, and green curves correspond to simulated changes $\mathcal{M}$, velocity effects $U_e$, and thermal driving effects $\Delta T_e$, respectively. In each of the plots, the black dashed line approximately corresponds to the calved length when the ice front sits approximately above the ridge crest.

ative anomalies (figure 13c–f). Melt rates do not change significantly in the first 'future' scenario (F1), in which the ice front is still located some way offshore of the ridge, in qualitative agreement with the idealized results. However, melt rates in the vicinity of the northern shear margin increase dramatically when the ice front is retreated to a position (F2) that sits (approximately) above the seabed ridge (figure 13d), and this region of enhanced melt rates extends almost all the way to the grounding line. With the ice front immediately above the seabed ridge, the outer cavity region no longer exists; this is reminiscent of the idealized results in which there is a qualitative change in the behavior when the outer cavity disappears and the only remaining regions of closed $f/h$ space are the inner cavity and the open ocean.

We show in figure 14a and b the mean melt rate as a function of calved length for the northern and southern inner cavity regions, respectively. In the northern inner cavity region, the mean melt rate remains approximately constant until the ice front approaches the seabed ridge. As the ice front approaches the ridge, the mean melt rate increases sharply, before remaining approximately constant as the ice front is retreated further. In the southern inner cavity region, the mean melt rate is less variable (in terms of percentage change, figure 14c), but the overall trend is that it increases while the ice front is located downstream of the seabed ridge, before dropping temporarily when the ice front is retreated to the ridge and subsequently increasing again. More quantitatively, the mean melt rate

in the northern inner cavity region reaches a peak that is approximately 12% larger than present day, which is first realized when the ice front is retreated to the ridge (figure 14c). Although the mean melt rate in the southern inner cavity region decreases when the ice front is retreated to the ridge (figure 14d), the melt rate in the entire inner cavity increases at this point (figure 14c). Indeed, the mean melt rate in the entire inner cavity increases approximately linearly after the first calving event (figure 14c).

Our interpretation of these results is guided by the idealized simulations presented in §3–6. The northern inner cavity region is shielded by a relatively narrow gap between the seabed ridge and the ice draft (figure 11c), and its melt response to calving behaves in a qualitatively similar way to idealized results with narrower gaps ($W \leq 150$ m). A velocity-thermal driving decomposition of these changes in melt rates (figure 14d) indicates that, as in the corresponding idealized case, both increases in thermal driving and velocity contribute to the increases in melt rate with calving while the ice front is located offshore of the ridge, and that a reduction in the boundary layer velocity is responsible for the decrease in melt rates when the ice front is retreated beyond the ridge. This suggests that the enhancement in melt rates with calving while the ice front is located offshore of the ridge is driven by increased heat reaching the inner cavity and a concomitant increase in buoyancy forcing and thus circulation strength. As in the idealized case, there is a change in behaviour when the calving front reaches the ridge, with the trend of increasing melt rate with calving reversed, although in this case it is experienced as a saturation of the melt rates, rather than a strong reduction, as in the idealized case. The melt rate is approximately independent of the ice front position once the ice front has retreated beyond the ridge, which is again in agreement with the idealized experiments.

The southern inner cavity region sits inshore of a relatively wide gap between the seabed ridge and the ice draft (figure 11). As was the case for idealized simulations with wide gaps ($W \geq 200$ m), the mean melt rate is less sensitive to the ice front position than it is with a narrow gap, i.e. for the northern inner cavity region (figure 14c). This reduced response is consistent with the corresponding idealized picture, in which depth-averaged flow is able to cross the ridge to supply warm water to the saturated inner cavity in each experiment, i.e. regardless of ice front position. This is borne out in figure 12, which indicates that depth-averaged flow is able to cross the ridge to the southern inner cavity in each of the idealized experiments. Thus calving only has limited influence.

## 8 Discussion

The results of the previous section suggest that the recent calving of PIG did not lead to increases in melting in either the shear margins or near the grounding line, which are particularly important for buttressing of the grounded ice sheet (Reese, Gudmundsson, et al., 2018). Our simulations therefore provide evidence that there will be no further buttressing losses associated with increased shelf melting as a result of the recent calving. Should this lack of response play out in practice, it might promote a negative feedback on ice shelf loss, encouraging its regrowth: the recent calving led to an acceleration of the grounded ice (Joughin et al., 2021), and thus an increase of the flux of ice into the shelf (assuming that ice thickness at the grounding line remained unchanged); a constant ice shelf mass balance can only be maintained if melting increases. The lack of increase in melting after the 2020 calving event might have, therefore, shifted the shelf mass balance towards positive, promoting regrowth of the ice shelf.

There is evidence (Lhermitte et al., 2020, for example) that damage to the PIIS has preconditioned it to break up and further ice front retreat is inevitable. Our experiments suggest that for any ice front position upstream of the present day position, further ice front retreat will result in an increase in melting. This suggests that the first chain in the calving-melt feedback loop (calving leads to increased melting and thus further

calving, or calving leads to increased melting, reduced buttressing, acceleration and damage and thus further calving) is never broken, supporting the possibility of such feedback processes occurring in West Antarctica. Investigating the detailed response of PIG to calving events would require the use of a coupled ice-ocean model, and is beyond the scope of this study. However, we do note here the complexity of this potential coupled response, highlighting two examples of processes involved (which themselves interact): firstly, an increase in melting would be expected to widen the gap between the ridge and the ice shelf base, relaxing the topographic barrier and thus potentially increasing the melt rate further, whilst simultaneously exposing the shelf to colder water, which might promote a reduction in melting. Secondly, if the ice shelf were to accelerate in response to enhanced melting, it be expected to experience dynamic thinning, with the potential to feed back on melting via geometric effects, as well as increasing the steady state calving rate, potentially resulting in ice shelf regrowth.

Our results suggest that the mean melt rate in the inner cavity will increase approximately linearly with calving beyond the 2020 front, and in particular, that the mean inner cavity melt rate will have increased by approximately 10% when the calving front sits above the ridge. A 10% increase in melt rates in the inner cavity region corresponds to an increased mass loss of approximately 3 Gt/year and could represent an important contribution to ice shelf mass imbalance. However, it should be noted this value reflects only changes in the inner cavity regions, which are a small fraction of the total ice shelf area; perhaps more important would be the effect of a 10% increase in melting in the vicinity of the grounding line, which is particularly important for buttressing the ice sheet. In addition, the spatial pattern of changes in melting indicates that these increases are often focused around the shear margins. The shear margins of Pine Island Ice Shelf are important for buttressing of the grounded ice sheet (De Rydt et al., 2021, for example), as well as being the areas most prone to damage and where cracks in ice shelves are often initiated, potentially triggering further calving. Thus, large melt anomalies in response to calving in these regions may have profound consequences for the grounded ice sheet. In addition, ice shelf thinning resulting from large melt anomalies in the shear margins of PIIS might result in enlargement of the basal channels which have been reported to exist there (Alley et al., 2019), thus localizing melting and further weakening the ice-shelf margins.

The magnitude of changes in melting in response to calving for the southern inner cavity region (for which the offshore ridge-seabed gap is wide) are similar to the corresponding idealized simulations, i.e. reasonably small. For the northern inner cavity region (narrow ridge-seabed gap), however, the magnitude of changes in melt with calving are smaller than the corresponding idealized experiments predict, even though the changes are qualitatively similar. We attribute this difference in magnitude to the complexities of the ice draft and seabed in the realistic simulations, as well as to our splitting of the inner cavity into two sub-regions, which relies on the assumption that they are entirely dynamically disconnected. Although a strong topographic barrier exists between them, some flow is able to cross this barrier, providing a connection between the two regions. This inner cavity decomposition is a convenient tool which permits us to account for some of the effect of the inhomogeneity in ridge-draft gap along its length, but further work is required to fully understand the role of variations in the ridge-draft gap in controlling basal melt rates on PIIS. It is also interesting to note that northern and southern inner cavity regions respond differently to the retreat, despite the exact same ocean conditions; their differing responses are only due to the different geometries and changes in ocean dynamics, highlighting again the importance of cavity geometry in controlling the melt response to calving.

The sensitivity of the melt response to the cavity geometry identified in the idealized simulations means that the observed response may in fact be somewhat different to that predicted here: if, for example, the ridge-draft gap is, in practice, smaller than

that used in our realistic simulations (there are reasonable uncertainties in the ice draft and bathymetry beneath the shelf), the melt response to calving might be significantly larger. Furthermore, the ice draft is not constant in time but is influenced by ice dynamics and mass balance; advection of thicker sections of the ice shelf to the ridge crest would, for example, be expected to narrow the ridge-draft gap and thus increase the sensitivity of melt rates to calving, and vice versa for the advection of thinner sections of ice. Our idealized simulations also suggest that the melt-gap geometric feedback identified by De Rydt et al. (2014), in which increases in the ridge-draft gap lead to an increase in the melt rate and thus further ridge-draft gap widening, holds for any ice front position offshore of the ridge. However, other geometric feedbacks not considered here may promote stabilization of the ice shelf. In particular, we speculate that the complex pattern of melt rate anomalies described in §7 might promote the formation of basal channels, for which there is evidence of an associated reduction in melt rates (Millgate et al., 2013, for example), thus potentially providing a stabilizing effect on the ice shelf.

On the decadal timescales on which ice sheets respond to perturbations in melting, variability in the depth of the pycnocline dominates ocean variability in the Amundsen Sea. Our idealized simulations point to a reduction in the sensitivity to pycnocline depth with calving once the ice front is reasonably close to the ridge provided that the gap is relatively thin ($l_c > 20$ km on the inset of figure 9a, which is appropriate for $W = 100$ m). However, for thicker gaps ($W > 150$ m), the sensitivity to pycnocline depth is largely independent of the ice front position (figure 9a, b). This conclusion is also borne out in our realistic experiments: supplementary experiments (not shown) using the realistic geometry, with the ocean restored to 2012 conditions in PIB far from the ice shelf, reveal that the ratio between the mean melt rate in the northern inner cavity region (narrow gap) with 2009 boundary conditions and the mean melt rate in the same region with 2012 boundary conditions is 1.52 for the largest ice shelf we consider, and 1.43 for the smallest. However, for the southern inner cavity region (wide gap), this ratio shows little change between the largest (1.29) and smallest (1.31) ice shelves we consider. The combination of a reduction in sensitivity in the northern box and an invariance in the southern box as calving proceeds suggests that PIIS melting may experience a reduction in the sensitivity to changes in ocean conditions in the Amundsen Sea in the future, assuming that the ice front continues to retreat. This motivates further study into future changes of the sensitivity of Amundsen Sea sector ice shelves to far field oceanic conditions.

It should also be noted that summer bias of observations means that the range of hydrographic conditions considered here is a lower bound: hydrographic conditions displaying either a thicker or thinner CDW layer may have occurred during seasons when sampling is not possible or prior to the observational record beginning. Our idealized simulations suggest that the melt response to calving is more sensitive in configurations featuring a thicker CDW layer in the boundary restoring profile (via a lower $P$ value); should calving occur at a moment when the CDW layer corresponds to a $P$ value beyond the range considered here, we might expect the melt response to calving to be larger than that described here (and vice versa for calving that occurs when the CDW layer is thinner than that considered here).

The results presented in this paper have implications for cavity scale melt rate parametrizations used in future projections of ice sheets and associated sea level rise. Such parametrizations take the ice shelf geometry and far field ocean conditions as inputs, and return a field of melt rates over the entire ice shelf, often by developing a conceptual model of the circulation within the cavity. At present, no such cavity scale melt rate parametrization is able to account for the position of the ice front, seabed topography, or indeed any BPV barrier, when computing the melt rate (Asay-Davis et al., 2017; Reese, Albrecht, et al., 2018; Bradley et al., 2022). Although the example of PIG is somewhat extreme in this BPV barrier sense, we have demonstrated that the combination of seabed ridge and ice

front position, which ultimately act as topographic BPV barriers, can exert an important control on the melt rate applied to an ice shelf. Ultimately, our results suggest that current cavity scale melt rate parametrizations must be improved to account for the seabed ridge if they are to be provide robust assessments of the future evolution of the Antarctic ice sheet.

It is important to note that MITgcm has a plethora of parameter choices and numerical settings, which might have an impact on the results of the experiments. These include choices of grid resolution, which are 400 m in the horizontal (to ensure mesoscale eddies are well resolved) and 10 m in the vertical. The same experiments ran at higher vertical resolution (5 m) did not change the results significantly, although results were somewhat different for lower resolution (20 m); this is perhaps unsurprising given that exchange over the ridge crest, which we have shown to be important in controlling the inner cavity melt rate, is expected to be sensitive to vertical resolution. Agreement with the higher resolution results gives us confidence that the experiments presented here reflect exchange processes over the ridge crest that are appropriately resolved.

Finally, it is important to note that forcing in our experiments comes exclusively from buoyancy fluxes associated with ice shelf melting and restoring at the boundaries. In particular, the experiments include neither surface heat and freshwater fluxes nor sea ice, which would be expected to alter the horizontal density gradients and thus circulation in the open ocean. In addition, they do not include wind stresses, which provide a leading order control on heat content and circulation in Pine Island Bay (Dutrieux et al., 2014), and have the potential to be particularly influential because wind driven currents are barotropic and thus more heavily influenced by topographic barriers.

## 9 Summary

The central aim of this study is to understand how, and why, melt rates on Pine Island Ice Shelf might respond to calving events that have already taken place recently, and those that might occur in the future. To address this question, we have performed numerical simulations in both an idealized domain, and one that is representative of PIIS.

The idealized experiments allowed us to isolate parametric dependencies in the melt response to calving, and elucidate the mechanisms responsible for it. We identified a sensitive dependency on the cavity geometry via the parameter $W$ that describes the gap between the seabed ridge and the ice draft: configurations with a narrow gap ($W \lesssim 150$ m) have a large response to calving, whereas those with wide gaps ($W > 150$ m) do not. We identified two key regimes for configurations whose cavities have narrow gaps: in the first regime, the ice front is located offshore of the ridge, and the inner cavity melt rate increases with calving, and the change in melting for a given calved length increases as the ice front approaches the ridge. In the second regime, the ice front is located at or inshore of the ridge, and melt rates are significantly reduced compared to when the ice front is just offshore of the ridge if the pycnocline is relatively high, or enhanced further if the pycnocline is relatively deep. In contrast, for configurations with wide gaps, the melt rate is largely independent of the location of the ice front. We identified the relative roles of changes in circulation and thermal driving in the melt response to calving, and described how these roles are modulated by depth-averaged flow across the ridge and topographic barriers in the domain. The results for wide gaps suggest that melt rates are insensitive to ice front position in ice shelf cavities with no seabed ridge. Although these idealized results are intended to inform our understanding of melt rate changes beneath Pine Island Glacier, they can also be considered to be an archetype for situations in which the seabed geometry restricts the access of warm water to the grounding line of an ice sheet.

The idealized experiments informed experiments performed using a cavity geometry that closely resembles PIIS, designed to assess how melt rates on PIIS might respond to calving in practice. This geometry has two inner cavity regions, which are approximately dynamically disconnected due to a thick ice keel across the center of the glacier. One of the inner cavity sections sits inshore of a narrow section of the ridge-draft gap; in this region the melt rate increases with calving while the ice front is located offshore of the ridge, before saturating with further calving beyond the ridge. In contrast, the other cavity section sits inshore of a wide section of the ridge-draft gap; there, the melt rate is largely independent of calving. Both of these observations are qualitatively consistent with the idealized simulations.

Our results demonstrate that the impact of calving on melt rates may represent an important, but as yet unexplored, contribution to the ice-ocean sensitivity of the West Antarctic Ice Sheet. They provide evidence that melt rates have not changed in response to recent calving events, but will increase linearly with future calving events. This increased mass loss, which is expected to take place in dynamically important regions of the ice shelf, might lead to a significant ice shelf mass imbalance. In addition, the constant increase in melt rate with retreat supports the possibility of feedback loops in which calving leads to increased melting and ultimately further calving.

**Acknowledgments**

A. T. B. and D. T. B. are supported by the NERC Grant NE/S010475/1. J. D. R. is supported by the TiPACCs project, which receives funding from the European Union's Horizon 2020 research and innovation programme under grant agreement no. 820575. NSF (through grant OPP-1643285) and the NASA MAP program provided support to P.D..

The simulations were performed using MITgcm at checkpoint c67u, which is publicly accessible at `http://mitgcm.org`. Files and code used to drive MITgcm and produce the figures in this paper are available at `https://github.com/alextbradley/PIG-calving-melt-response`.

The numerical simulations were carried out on ARCHER2, the U.K. national HPC facility (`http://archer2.ac.uk/`).

## References

Alley, K. E., Scambos, T. A., Alley, R. B., & Holschuh, N. (2019). Troughs developed in ice-stream shear margins precondition ice shelves for ocean-driven breakup. *Sci. Adv*, *5*(10), eaax2215.

Arthern, R. J., & Williams, C. R. (2017). The sensitivity of west antarctica to the submarine melting feedback. *Geophys. Res. Lett.*, *44*(5), 2352–2359.

Asay-Davis, X. S., Jourdain, N. C., & Nakayama, Y. (2017). Developments in simulating and parameterizing interactions between the southern ocean and the antarctic ice sheet. *Curr. Clim. Ch. Rep.*, *3*(4), 316–329.

Bradley, A. T., Williams, C. R., Jenkins, A., & Arthern, R. (2022). Asymptotic analysis of subglacial plumes in stratified environments. *Proc. Roy. Soc. A*, *478*(2259), 20210846. doi: 10.1098/rspa.2021.0846

Dansereau, V., Heimbach, P., & Losch, M. (2014). Simulation of subice shelf melt rates in a general circulation model: Velocity-dependent transfer and the role of friction. *Journal of Geophysical Research: Oceans*, *119*(3), 1765–1790.

De Rydt, J., & Gudmundsson, G. H. (2016). Coupled ice shelf-ocean modeling and complex grounding line retreat from a seabed ridge. *J. Geophys. Res. Earth Surf.*, *121*(5), 865-880.

De Rydt, J., Holland, P. R., Dutrieux, P., & Jenkins, A. (2014). Geometric and oceanographic controls on melting beneath pine island glacier. *J. Geophys.*

*Res. Oceans*, *119*(4), 2420–2438.

De Rydt, J., Reese, R., Paolo, F. S., & Gudmundsson, G. H. (2021). Drivers of pine island glacier speed-up between 1996 and 2016. *Cryosphere*, *15*(1), 113–132.

Dutrieux, P., De Rydt, J., Jenkins, A., Holland, P. R., Ha, H. K., Lee, S. H., ... Schröder, M. (2014). Strong sensitivity of pine island ice-shelf melting to climatic variability. *Science*, *343*(6167), 174–178.

Dutrieux, P., Vaughan, D. G., Corr, H. F. J., Jenkins, A., Holland, P. R., Joughin, I., & Fleming, A. H. (2013). Pine island glacier ice shelf melt distributed at kilometre scales. *Cryosphere*, *7*(5), 1543–1555.

ESA. (2020). *Copernicus sentinel data 2020.*

Gagliardini, O., Durand, G., Zwinger, T., Hindmarsh, R. C. A., & Le Meur, E. (2010). Coupling of ice-shelf melting and buttressing is a key process in ice-sheets dynamics. *Geophys. Res. Lett.*, *37*(14).

Gardner, A. S., Moholdt, G., Scambos, T., Fahnstock, M., Ligtenberg, S., van den Broeke, M., & Nilsson, J. (2018). Increased west antarctic and unchanged east antarctic ice discharge over the last 7 years. *Cryosphere*, *12*(2), 521–547.

Goldberg, D. N., Gourmelen, N., Kimura, S., Millan, R., & Snow, K. (2019). How accurately should we model ice shelf melt rates? *Geophys. Res. Lett.*, *46*(1), 189–199.

Grosfeld, K., Gerdes, R., & Determann, J. (1997). Thermohaline circulation and interaction between ice shelf cavities and the adjacent open ocean. *J. Geophys. Res. Oceans*, *102*(C7), 15595–15610.

Gudmundsson, G. H. (2013). Ice-shelf buttressing and the stability of marine ice sheets. *The Cryosphere*, *7*(2), 647–655.

Gudmundsson, G. H., Paolo, F. S., Adusumilli, S., & Fricker, H. A. (2019). Instantaneous antarctic ice sheet mass loss driven by thinning ice shelves. *Geophys. Res. Lett.*, *46*(23), 13903–13909.

Heimbach, P., & Losch, M. (2012). Adjoint sensitivities of sub-ice-shelf melt rates to ocean circulation under the pine island ice shelf, west antarctica. *Ann. Glaciol.*, *53*(60), 59–69.

Heywood, K. J., Biddle, L. C., Boehme, L., Dutrieux, P., Fedak, M., Jenkins, A., ... M, W. B. G. (2016). Between the devil and the deep blue sea: The role of the amundsen sea continental shelf in exchanges between ocean and ice shelves. *Oceanography*, *29*(4), 118–129.

Holland, D. M., & Jenkins, A. (1999). Modeling thermodynamic ice–ocean interactions at the base of an ice shelf. *J. Phys. Oceanogr.*, *29*(8), 1787–1800.

Jackson, L., Hughes, C. W., & Williams, R. G. (2006). Topographic control of basin and channel flows: The role of bottom pressure torques and friction. *J. Phys. Oceanogr.*, *36*(9), 1786–1805.

Jacobs, S. S., Hellmer, H. H., & Jenkins, A. (1996). Antarctic ice sheet melting in the southeast pacific. *Geophys. Res. Lett.*, *23*(9), 957–960.

Jacobs, S. S., Jenkins, A., Giulivi, C. F., & Dutrieux, P. (2011). Stronger ocean circulation and increased melting under pine island glacier ice shelf. *Nat. Geosci.*, *4*(8), 519–523.

Jacobs, S. S., Jenkins, A., Hellmer, H., Giulivi, C., Nitsche, F., Huber, B., & Guerrero, R. (2015). The amundsen sea and the antarctic ice sheet. *Oceanography*, *25*(3), 154–163.

Jenkins, A., Dutrieux, P., Jacobs, S. S., McPhail, S. D., Perrett, J. R., Webb, A. T., & White, D. (2010). Observations beneath pine island glacier in west antarctica and implications for its retreat. *Nat. Geosci.*, *3*(7), 468–472.

Jenkins, A., Shoosmith, D., Dutrieux, P., Jacobs, S., Kim, T. W., Lee, S. H., ... Stammerjohn, S. (2018). West antarctic ice sheet retreat in the amundsen sea driven by decadal oceanic variability. *Nat. Geosci.*, *11*(10), 733–738.

Joughin, I., Shapero, D., Smith, B., Dutrieux, P., & Barham, M. (2021). Ice-shelf retreat drives recent pine island glacier speedup. *Sci. Adv.*, *7*(24), eabg3080.

Joughin, I., Smith, B. E., & Holland, D. M. (2010). Sensitivity of 21st century sea level to ocean-induced thinning of pine island glacier, antarctica. *Geophys. Res. Lett.*, *37*(20).

Korona, J., Berthier, E., Bernard, M., Rémy, F., & Thouvenot, E. (2009). Spirit. spot 5 stereoscopic survey of polar ice: reference images and topographies during the fourth international polar year (2007–2009). *ISPRS J. Photogramm. Remote Sens.*, *64*(2), 204–212.

Lhermitte, S., Sun, S., Shuman, C., Wouters, B., Pattyn, F., Wuite, J., ... Nagler, T. (2020). Damage accelerates ice shelf instability and mass loss in amundsen sea embayment. *Proc. Nat. Acad. Sci.*, *117*(40), 24735–24741.

Liu, Y., Moore, J. C., Cheng, X., Gladstone, R. M., Bassis, J. N., Liu, H., ... Hui, F. (2015). Ocean-driven thinning enhances iceberg calving and retreat of antarctic ice shelves. *Proc. Nat. Acad. Sci.*, *112*(11), 3263–3268.

Losch, M. (2008). Modeling ice shelf cavities in z coordinate ocean general circulation model. *J. Geophys. Res. Oceans*, *113*(C8).

Marshall, J., Hill, C., Perelman, L., & Adcroft, A. (1997). Hydrostatic, quasi-hydrostatic, and nonhydrostatic ocean modeling. *Journal Geophys. Res. Oceans*, *102*(C3), 5733–5752.

McDougall, T. J., Jackett, D. R., Wright, D. G., & Feistel, R. (2003). Accurate and computationally efficient algorithms for potential temperature and density of seawater. *J. Atmos. Ocean. Technol.*, *20*(5), 730–741.

Mertz, G., & Wright, D. G. (1992). Interpretations of the jebar term. *Journal of Physical Oceanography*, *22*(3), 301–305.

Millgate, T., Holland, P. R., Jenkins, A., & Johnson, H. L. (2013). The effect of basal channels on oceanic ice-shelf melting. *J. Geophys. Res. Oceans*, *118*(12), 6951–6964.

Mouginot, J., Rignot, E., & Scheuchl, B. (2014). Sustained increase in ice discharge from the amundsen sea embayment, west antarctica, from 1973 to 2013. *Geophys. Res. Lett.*, *41*(5), 1576–1584.

Pacanowski, R., & Philander, S. (1981). Parameterization of vertical mixing in numerical models of tropical oceans. *J. Phys. Oceanogr.*, *11*(11), 1443–1451.

Patmore, R. D., Holland, P. R., Munday, D. R., Naveira Garabato, A. C., Stevens, D. P., & Meredith, M. P. (2019). Topographic control of southern ocean gyres and the antarctic circumpolar current: a barotropic perspective. *J. Phys. Oceanogr.*, *49*(12), 3221–3244.

Pettit, E., Wild, C., Alley, K., Muto, A., Truffer, M., Bevan, S., ... Benn, D. (2021, December). Collapse of Thwaites Eastern Ice Shelf by intersecting fractures. In *Agu fall meeting abstracts.*

Pritchard, H. D., Ligtenberg, S. R. M., Fricker, H. A., Vaughan, D. G., van den Broeke, M. R., & Padman, L. (2012). Antarctic ice-sheet loss driven by basal melting of ice shelves. *Nature*, *484*(7395), 502–505.

Reese, R., Albrecht, T., Mengel, M., Asay-Davis, X., & Winkelmann, R. (2018). Antarctic sub-shelf melt rates via pico. *The Cryosphere*, *12*(6), 1969–1985.

Reese, R., Gudmundsson, G. H., Levermann, A., & Winkelmann, R. (2018). The far reach of ice-shelf thinning in antarctica. *Nat. Clim. Chang.*, *8*(1), 53–57.

Rignot, E. (2008). Changes in west antarctic ice stream dynamics observed with alos palsar data. *Geophy. Res. Lett.*, *35*(12).

Rignot, E., Jacobs, S., Mouginot, J., & Scheuchl, B. (2013). Ice-shelf melting around antarctica. *Science*, *341*(6143), 266–270.

Rignot, E., Mouginot, J., Morlighem, M., Seroussi, H., & Scheuchl, B. (2014). Widespread, rapid grounding line retreat of pine island, thwaites, smith, and kohler glaciers, west antarctica, from 1992 to 2011. *Geophys. Res. Lett.*, *41*(10), 3502–3509.

Rignot, E., Mouginot, J., & Scheuchl, B. (2011). Ice flow of the antarctic ice sheet. *Science*, *333*(6048), 1427–1430.

Rignot, E., Mouginot, J., Scheuchl, B., Van Den Broeke, M., Van Wessem, M. J., & Morlighem, M. (2019). Four decades of antarctic ice sheet mass balance from 1979–2017. *Proc. Nat. Acad. Sci.*, *116*(4), 1095–1103.

Rignot, E., Vaughan, D. G., Schmeltz, M., Dupont, T., & MacAyeal, D. (2002). Acceleration of pine island and thwaites glaciers, west antarctica. *Ann. Glac.*, *34*, 189–194.

Seroussi, H., Morlighem, M., Larour, E., Rignot, E., & Khazendar, A. (2014). Hydrostatic grounding line parameterization in ice sheet models. *The Cryosphere*, *8*(6), 2075–2087.

Shepherd, A., Wingham, D., & Rignot, E. (2004). Warm ocean is eroding west antarctic ice sheet. *Geophys. Res. Lett.*, *31*(23).

Smith, J. A., Andersen, T. J., Shortt, M., Gaffney, A. M., Truffer, M., Stanton, T. P., ... Vaughan, D. G. (2017). Sub-ice-shelf sediments record history of twentieth-century retreat of pine island glacier. *Nature*, *541*(7635), 77–80.

St-Laurent, P., Klinck, J., & Dinniman, M. (2015). Impact of local winter cooling on the melt of pine island glacier, antarctica. *J. Geophys. Res: Oceans*, *120*(10), 6718–6732.

Sun, S., Cornford, S. L., Moore, J. C., Gladstone, R., & Zhao, L. (2017). Ice shelf fracture parameterization in an ice sheet model. *The Cryosphere*, *11*(6), 2543–2554.

Webber, B. G., Heywood, K. J., Stevens, D. P., Dutrieux, P., Abrahamsen, E. P., Jenkins, A., ... Kim, T. W. (2017). Mechanisms driving variability in the ocean forcing of pine island glacier. *Nat. Commun.*, *8*(1), 1–8.

Yoon, S.-T., Lee, W. S., Nam, S., Lee, C.-K., Yun, S., Heywood, K., ... Bradley, A. T. (2022). *Meltwater feedback reduces ocean heat input to an antarctic ice shelf* (Vol. 13) (No. 306).